

Structure and energetics of cation-water complex confined in
Fluorohectorite. A DFT/DFTB computational study

Mustafa Ali Hadi Jarallah

Master's thesis in Applied Physics and Mathematics

Trondheim, July 10, 2020

Abstract

The present work reports a first principle study based on DFT and the tight-binding method DFTB, of the monovalent cations (Li^+ , Na^+ and K^+) and the divalent cations (Be^{2+} , Mg^{2+} and Ca^{2+}) intercalated in fluorohectorite. Considering the $\text{Li}^+/\text{Mg}^{2+}$ octahedral substitution and the hypothetical case with $\text{Na}^+/\text{Mg}^{2+}$. An important property of this smectite clay is the ability to adsorb water and thereby swell several times the initial thickness. The microscopic behavior of the underlying crystalline swelling was investigated for the chosen cations and by systematically increasing the water content in the interlayer. The simulation predicts that a $\text{H}_2\text{O}/\text{M}^{n+}$ ratio of 2 and 4 corresponding to the stable 1WL and 2WL states respectively. The simulated d_{001} spacings for 1WL and 2WL for the monovalent cations are in remarkable agreement with experimental data. While this value for the 2WL divalent cations was consistently low, indicating a low coordination number. The microscopic interlayer structure revealed that for 1WL, Na^+ resides in the middle of the plane shifted towards the hexagonal cavity, in an inner-sphere coordination by both surfaces. While the case for K^+ and Ca^{2+} showed inner-sphere coordination by only the basal surface. The interlayer environments for Ca^{2+} and Na^+ changed significantly upon hydration in the 2WL state, with only outer-sphere coordination to the basal surface, displaced in the middle plane above the Si tetrahedra. In contrast K^+ remains in an inner-sphere coordination, acting as swelling inhibitor. Reflecting that K^+ screens the negatively charged hexagonal cavity, and hence weakens the repulsion between the clay sheets. Which is in agreement with previous experiments and simulations. The experimental fitted dispersion correction D3(BJ) shifts the d_{001} spacing consistently to lower values, and only improves the swelling constant for the 1WL state. The simulation are in good agreement with previous experimental and simulation work of hectorite, showing that the swelling process depends on the cations hydration energy, ionic radius, and the type of substitution controlling the charge distribution on the hexagonal cavity.

Sammendrag

Denne oppgaven er basert på simuleringer gjennomført med tetthetsfunksjonalteori (DFT) og tetthetsfunksjonalteori tight-binding (DFTB) av de monovalente- (Li^+ , Na^+ and K^+) og de divalente kationene (Be^{2+} , Mg^{2+} and Ca^{2+}) interkalert i fluorohektoritt. Med følgende oktaederiske substitusjon $\text{Li}^+/\text{Mg}^{2+}$ og det hypotetiske tilfellet $\text{Na}^+/\text{Mg}^{2+}$. En viktig egenskap med denne type leiere er evnen til å adsorbere vann og dermed svulle flere ganger den opprinnelige tykkelsen. De mikroskopiske egenskapene til den underliggende krystallinske svellingen ble undersøkt for de valgte kationene ved systematisk økning av antallet vann i mellomlaget. Dette resulterte til et $\text{H}_2\text{O}/\text{M}^{n+}$ forhold på 2 og 4 for de tilsvarende stabile 1WL and 2WL tilstandene. Den simulerte d_{001} avstanden for de monovalente kationene viste en presis overensstemmelse med eksperimentelle data. Den mikroskopiske mellomlagstrukturen viste at Na^+ for 1WL befinner seg i midten av planet forskjøvet mot det heksagonalet hulrommet, i en indre-sfære koordinasjon av begge overflater. Mens tilfellet for K^+ og Ca^{2+} viste en indre-sfære koordinasjon av kun basaloverflaten. Koordinasjonen i mellomlaget endret seg betydelig for Ca^{2+} og Na^+ for 2WL tilstanden, med kun ytre-sfære koordinering til basaloverflaten, og forskyvning over Si tetraedet. I motsetning forblir K^+ i en indre-sfære koordinering og fungerer som svelle-hemmende. Dette kan forklares ved at K^+ kationet skjermes det negativt ladede heksagonalet hulrommet og dermed svekker frastøtingene mellom leiereoverflatene. Dette er i samsvar med tidligere eksperimenter og simuleringer. Den eksperimentell baserte Van der Waals korreksjonen D3(BJ) systematisk forskyver d_{001} avstanden til kortere avstander, og dermed kun forbedrer svellekonstanten for 1WL tilstanden. Simuleringene er i overensstemmelse med tidligere eksperimenter og simuleringer av hektoritt, og viser at svulle prosessen avhenger av kationets hydrasjonsenergi, ionetradien og type substitusjon som kontrollerer ladningsfordelingen over det heksagonalet hulrommet.

Preface

This thesis will mark the end of the five year master program in applied physics and mathematics at the Norwegian University of Science and Technology(NTNU). The entirety of the work presented in this thesis was carried out during the spring of 2020. The idea was presented to me by Prof. Jon Andreas Støvneng in collaboration with Laboratory for Soft and Complex Matter studies.

I would like to give a special thanks to Prof. Jon Andreas Støvneng for all the friendly discussions, insight and patience during the thesis. Special thanks to Rasoul for introducing me to density functional theory during the specialization project. My thanks are extended the SCM support team, which have given quick and excellent feedback to my questions. I would also like thank Kristoffer and Siv-Marie for the insight to the world of clay. Finally, I would like to thank my family for the endless support and motivation.

Contents

Abstract	i
Sammendrag	i
Preface	ii
Table of Contents	iv
List of Tables	vi
List of Figures	viii
Abbreviations	ix
1 Introduction	1
1.1 Fluorohectorite	2
1.2 The present work	3
1.2.1 Structure of the report	3
2 Electronic Structure Theory	5
2.1 The Many-body Equation	5
2.1.1 Hartree method	6
2.1.2 Hartree-Fock method	7
2.2 The foundations of DFT	8
2.3 The Kohn-Sham equations	8
2.4 The exchange-correlation functional	10
2.5 Calculation scheme	10
2.6 Hellmann-Feynman forces	12

2.7	Dispersion correction	12
2.8	Computational approaches to DFT	13
2.8.1	Reciprocal space and Bloch's theorem	13
2.8.2	k-point sampling	13
2.8.3	Convergence	14
2.9	Potential energy surface	14
2.10	Review of SCC-DFTB	14
3	Computational details	17
3.1	Geometry optimization	17
3.1.1	Fast Inertial Relaxation Engine	18
3.2	Mulliken charge analysis	19
3.3	Bader charge analysis	19
4	Results and Discussion	21
4.1	Testing functionals	21
4.2	Hydrated cations	23
4.2.1	Geometrical parameters	23
4.2.2	Bonding energy of cation-water complex	27
4.3	Structure of hydrated Fluorohectorite	32
4.4	Surface charges	36
4.5	1WL- and 2WL basal spacing	37
4.5.1	Basal spacing for Fh_{Na}	43
4.6	M^{n+} -H ₂ O Interlayer Structure	47
5	Conclusion	55
5.1	Concluding remarks	55
5.2	Future work	56
	Bibliography	57

List of Tables

4.1	Calculated M-O distance for different methods.	22
4.2	Mulliken charge analysis for the monohydrated cations compared with the single water molecule. And the effect on the O-H distance. Calculated at the DFT level.	25
4.3	Mulliken charge analysis for the monohydrated cations compared with the single water molecule. And the effect on the O-H distance. Calculated at the SCC-DFTB level.	25
4.4	Common experimental values of ionic properties associated with clay interaction, given in [1]. Experimental hydration number are given in parentheses.	31
4.5	Partial charges of Cations on dry Fh_{Li} . And the average partial charges of Si and O on the interlayer surface. Calculated using Bader charge analysis.	37
4.6	Partial charges of Cations on dry Fh_{Na} . And the average partial charges of Si and O on the interlayer surface. Calculated using Bader charge analysis.	37
4.7	Swelling constant d_{001} of Fh_{Li} for the dry, 1WL and 2WL respectively. Without D3(BJ) dispersion correction.	42
4.8	Swelling constant d_{001} of Fh_{Li} for the dry, 1WL and 2WL respectively. With D3(BJ) dispersion correction. Experimental- and simulated work from previous studies are also included.	42
4.9	Swelling constant d_{001} of Fh_{Na} for the dry, 1WL and 2WL respectively. Without D3(BJ) dispersion correction.	46
4.10	Swelling constant d_{001} of Fh_{Na} for the dry, 1WL and 2WL respectively. With D3(BJ) dispersion correction.	46
4.11	Data of Na^+ , K^+ and Ca^{2+} coordination structure in dry, 1WL and 2WL Fh_{Li} . Without D3(BJ) dispersion.	53
4.12	Data of Na^+ , K^+ and Ca^{2+} coordination structure in dry, 1WL and 2WL Fh_{Li} . With D3(BJ) dispersion correction.	53

List of Figures

1.1	Schematic 2:1 fluorohectorite structure with tetrahedral(T_h)- and octahedral(O_h) layers, left Figure. Right Figure shows the snapshot of the Li^+/Mg^{2+} substitution, the basal oxygen and the interlayer Na^+ cation. Color code used throughout this thesis, Na:white, Li:grey, O:red, F:green, Si:gold and Mg:purple.	2
2.1	Flow-chart for solving the Kohn-Sham equations 2.18 in a self-consistent scheme. The loop terminates when the desired density and the previous density differ by less than a user defined tolerance, adapted from [2]. . . .	11
4.1	Bonding energy comparison of $Li^+(H_2O)$ complex for the LDA, PW91, PBE, revPBE and revPBE-D3 XC-functionals. The latter functional include dispersion correction D3.	22
4.2	The M-O distance variation with charge and size for the monohydrated cation, using DFT-revPBE and the two tight-binding methods SCC-DFTB and GFN1-xTB.	23
4.3	The H-O-H angle variation with charge and size for the monohydrated cation compared to the isolated H_2O molecule, using DFT-revPBE and the two tight-binding methods SCC-DFTB and GFN1-xTB.	24
4.4	The displacement of the electron density depicted by the change in the HOMO orbital. The upper row is the HOMO for the single water molecule and the lower row is for $Be^{2+}(H_2O)$	26
4.5	Configurations of the hydrated Li^+ -complex, and the special case for $Be(H_2O)_5^{2+}$ and $Ca(H_2O)_2^{2+}$. The geometry of the configuration is indicated underneath.	26
4.6	Correlation of the bonding energy for the cation-complex given by DFT and SCC-DFTB.	27

4.7	Bonding energy of cation-water complex using DFT-revPBE (upper graph) and SCC-DFTB (lower figure), showing the trends when changing the size and charge of the cation.	29
4.8	Correlation of the bonding energy and square of the reciprocal M-O distance for the cation-complex given by DFT(upper graph) and SCC-DFTB(lower graph).	30
4.9	Cation properties associated with clay interaction, experimental values are given in [1].	31
4.10	Snapshots of the simulated dry Na-Fh _{Li} , viewed from xz-plane in the left structure and the repeated unit cell in the righth, viewed from the xy-plane.	32
4.11	Snapshots of the simulated 1WL Na-Fh _{Li} , viewed from xz-plane in the left structure and the repeated unit cell in the righth, viewed from the xy-plane.	33
4.12	Snapshots of the simulated 2WL Na-Fh _{Li} , viewed from xz-plane in the left structure and the repeated unit cell in the righth, viewed from the xy-plane.	33
4.13	Change of lattice parameters upon hydration for the 1WL Na-Fh _{Na} case. Upper graph shows the change in the lattice vectors. While the lower figure measures the relative error from 90° for the lattice angles.	34
4.14	The lattice vectors for plain fluorohectorite.	35
4.15	Swelling constant d_{001} (Å) 1WL Fh _{Li} as a function of water molecules.	38
4.16	Bonding energy of 1WL cation-Fh _{Li} as a function of water molecules.	39
4.17	Swelling constant d_{001} (Å) of 2WL Fh _{Li} as a function of water molecules.	40
4.18	Bonding energy of 2WL cation-Fh _{Li} as a function of water molecules.	41
4.19	Swelling constant d_{001} (Å) of 1WL Fh _{Na} as a function of water molecules.	43
4.20	Bonding energy of 1WL cation-Fh _{Na} as a function of water molecules.	44
4.21	Swelling constant d_{001} (Å) of 2WL Fh _{Na} as a function of water molecules.	45
4.22	Bonding energy of 2WL cation-Fh _{Na} as a function of water molecules.	46
4.23	Geometry of dry Fh _{Li} with Na, K and Ca in the interlayer.	48
4.24	Geometry of 1WL Fh _{Li} with Na, K and Ca in the interlayer.	50
4.25	Geometry of 2WL Fh _{Li} with Na, K and Ca in the interlayer.	52

Abbreviations

XC	Exchange-Correlation
DFT	Density Functional Theory
DFTB	Density Functional Tight-Binding
LDA	Local Density Approximation
GGA	Generalized Gradient Approximation
NAO	Natural Atomic Orbitals
STO	Slater Type Orbitals
TS	Transition State
TZP	Triple Zeta Polarization
PBE	Perdew-Burke-Ernzerhof
revPBE	revised Perdew-Burke-Ernzerhof
QUASINANO2015	QN15

Introduction

Clay minerals are abundant, non-toxic and reusable. Making up 10% of the Earth's volume, these layered nanoporous aluminosilicates find numerous structures, properties and man-made applications [3, 4, 5]. The high retention capacity makes them major components in geochemical and environmental situations [6]. For instance they are considered as very promising host for nuclear waste disposal [7], deep CO₂ storage and for reactive transport [6, 8]. Their adsorption capacity and ion exchange properties have made them efficient drug carriers for long lasting drug concentrations [9]. For all aluminosilicates the unit cell consists of TO₄ tetrahedra (T = Si, Al) and XO₆ octahedra (X = Mg, Al, Fe,...) by combining the edges and corners results in a multitude of structures. Ranging from the arrangement of two-dimensional layers in clays to the formation of cavities and channels in zeolites [10]. Clay minerals are crystalline layers connected by sharing the corners of TO₄ tetrahedra and edge shared XO₆ octahedra, left structure in Figure 1.1.

Smectite clay is particularly important due to their ability to adsorb water in their interlayer space, and thus expand several times from their initial thickness. This swelling behavior is controlled by the interaction of confined water molecules and the charge compensating cations in the interlayer, see the right structure in Figure 1.1. In recent years, the structure and dynamics of water and cations in the interlayer have been studied extensively by several experimental techniques. Such as X-ray diffraction (XRD), quasi-elastic neutron scattering (QENS) and nuclear magnetic resonance (NMR) [11, 12]. Revealing that the structure, dynamics and energetics are strongly controlled by the different interlayer cations and their hydration energies. Due to the large unit cells of crystalline silicates consisting of ~100 atoms, and the low symmetry of the lattices. The experiments have resulted in unambiguous interpretations. Therefore molecular modelling of these complex host-guest systems have become an important tool to understand the macroscopic properties with its behavior at the atomic level [10]. Hence this challenging problem was approached using the field of computational quantum mechanics by solving the time-independent Schrodinger equation at the level of *Density Function Theory* (DFT) and at the semi-empirical tight-binding method (DFTB).

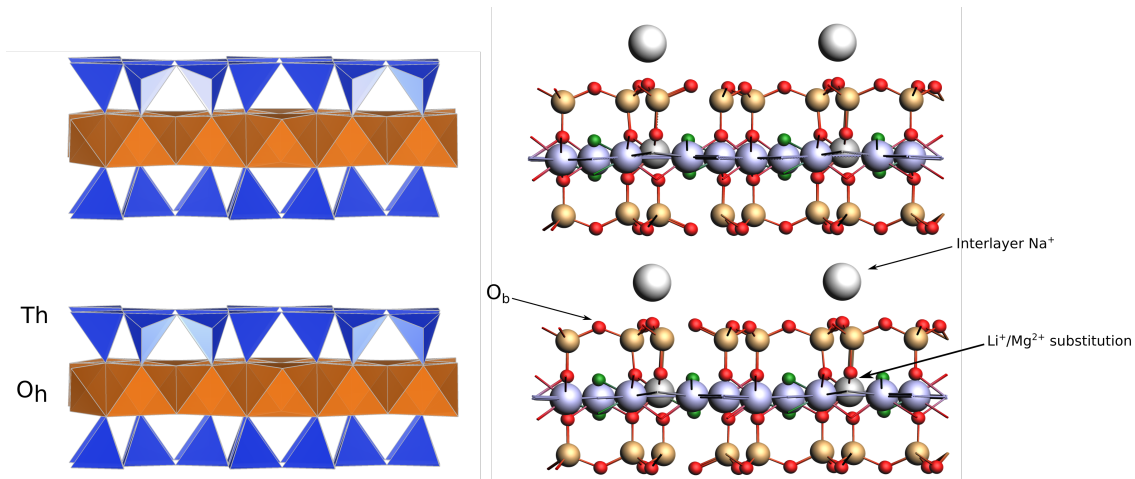


Figure 1.1: Schematic 2:1 fluorohectorite structure with tetrahedral(T_h)- and octahedral(O_h) layers, left Figure. Right Figure shows the snapshot of the Li^+/Mg^{2+} substitution, the basal oxygen and the interlayer Na^+ cation. Color code used throughout this thesis, Na:white, Li:grey, O:red, F:green, Si:gold and Mg:purple.

1.1 Fluorohectorite

The smectite clay modelled during this work is fluorohectorite (Fh). The purity of composition of this synthetic clay, contribute to an improved and consistent study of the interlayer galleries compared with natural clay minerals. Fluorohectorite is a 2:1 layer silicate, where two tetrahedral silicate layer sandwiching an octahedral metal layer, abbreviated as TOT structure, see left structure Figure 1.1. Where fraction of Mg^{2+} in the octahedral layer are substituted by Li^+ , depicted in the right structure in Figure 1.1. The hypothetical case with Na^+/Mg^{2+} substitution is also considered, for further insight on how this substitution effect the charge distribution of the basal oxygens(O_b). This net negative charge in the TOT layer is compensated by charge-balancing cations in the interlayer Figure 1.1. In this thesis several interlayer cations with different properties have been compared, such as Li^+ , Na^+ , K^+ , Be^{2+} , Mg^{2+} and Ca^{2+} . The Fh model is based on the structure by Kalo et al. [13] and belongs to monoclinic crystal system with $C2/m$ symmetry [14], given by the formula

$$M_y(Mg_{6-y}Li_y)Si_8O_{20}F_4 \quad (1.1)$$

such that the unit cell contains 38 atoms. The octahedral Li^+/Mg^{2+} is given by the ratio of 1/5 for the monovalent cations and 2/4 for divalent cations. Compensated by the M^{n+} cations, for $n=1,2$.

1.2 The present work

The objective of the following work is to give comprehensive description of the formation of the cation-water complex, to illustrate the effect of cation hydration energy upon the swelling phenomenon. Characterize the coordination and energetics of the cations in the interlayer galleries of fluorohectorite as the water content is increased systematically. And to gain simple insight on how well does the DFTB method model weak interaction between the clay sheets.

1.2.1 Structure of the report

The theory behind DFT and DFTB will be introduced in chapter 2, then chapter 3 states the computational details employed during this work. Where in chapter 4 the results and discussion will be presented. Finally chapter 5 ends with concluding remarks and thoughts on future work.

Electronic Structure Theory

The traditional methods for solving the many-body problem based on the wave function encounter an exponential wall, which means that the complexity of the solution increases exponentially with the size of the system[15]. Therefore method of DFT have shown to provide a fine balance between accuracy and computational cost. DFT computational time rises moderately with the number of atoms, $T \sim N^\alpha$, for $\alpha \approx 1-3$ [16]. This chapter gives a brief introduction to the electronic structure theory approached by DFT. And for the purpose of bulk calculations the density functional tight-binding SCC-DFTB is introduced [17, 18, 19].

2.1 The Many-body Equation

The general picture of condensed-matter physics contains a given material built up from electrons and at most few hundred kinds of nuclei with an electrostatic interaction. The electrons at positions \mathbf{r}_i attracted to the nuclei of charge Z at positions \mathbf{R}_μ , a pair of electrons repel one another, and two nuclei repel one another. All given by the basic Coulombic interaction. The heavy nuclei regarded as classical particles, while the electrons must be described by quantum mechanics. Since the important valence electrons in most elements move at speeds much less than the speed of light, the distribution of the electron states are governed by the non-relativistic equation for the many-electron wave function Ψ . Described by the time-dependent Schrödinger equation

$$i\hbar \frac{\partial}{\partial t} \Psi(\{\mathbf{r}_i\}, \{\mathbf{R}_\mu\}, t) = H\Psi(\{\mathbf{r}_i\}, \{\mathbf{R}_\mu\}, t) \quad (2.1)$$

where $\{\mathbf{R}_\mu\}$ and $\{\mathbf{r}_i\}$ are the sets of nuclei- and electron positions(spatial and spin) respectively. H is the Hamiltonian of the system, and t is the time. In the spirit of the Born-Oppenheimer approximation, the dynamics of the electron and nuclei are separated

by considering a much heavier nuclei, thus fixed while solving for the electrons[20]¹. The Coulomb potential of the nuclei acts now as an external electrostatic field. Thus focusing on the Hamiltonian for the electrons, where the positions of the nuclei are parameters. This reduces the problem to solving the time-independent Schrödinger equation,

$$\left[\sum_{i=1}^N -\frac{1}{2} \nabla_i^2 - \sum_j \frac{Z_l}{|\mathbf{r}_i - R|} + \frac{1}{2} \sum_{i \neq j} \frac{1}{|\mathbf{r}_i - \mathbf{r}_j|} + V_{ext} \right] \Psi_R(r) = E(R) \Psi_R(r) \quad (2.2)$$

The left hand side includes from the left, the electron kinetic energy T_e , the Coulomb attraction between electrons and nuclei V , the Coulomb repulsion between the electrons V_{ee} , and V_{ext} some external potential, for instance the electromagnetic field. Using Hartree atomic units² where the conventional fundamental constants, $\hbar = m_e = e = 4\pi\epsilon_0 = 1$, and should be used throughout. For a given position R of the nuclei one obtains $E(R)$, the *potential energy surface* (PES). Where $E(R)$ determines the nuclear motion, see section 2.9 for further explanation. Assuming closed-shell systems, where the total spins of the system is zero. Furthermore seeking only global minimum, hence the zero temperature equilibrium state for the electrons. Because electrons are fermions they have to obey the Pauli exclusion principle, where each allowed energy state is filled with exactly two electrons with opposite spins. Thus the only physical solutions of 2.2 has to obey the following

$$P_{ij} \Psi = -\Psi \quad (2.3)$$

where the P_{ij} operator permutes the position and spin coordinates of electrons i and j . Solving equation 2.2 is equivalent to finding the ground state by the variational principle using the method of Lagrange multipliers

$$\delta \{ \langle \Psi | H | \Psi \rangle - E \langle \Psi | \Psi \rangle \} = 0 \quad (2.4)$$

The challenging part of solving equation 2.2 is the interaction between the electrons. The usual approach forward is the mean-field approximation by Hartree[21], where the electrons are single particle states interacting via an average potential. And further extended by Fock to the well known Hartree-Fock method.

2.1.1 Hartree method

In the Hartree approximation[21] the wave function takes the form as a product of non-interacting single particle states $\phi_i(\mathbf{r}_i)$,

$$\Psi(\{\mathbf{r}_i\}) = \prod_i^N \phi_i(\mathbf{r}_i) \quad (2.5)$$

¹Meaning that the electrons respond faster to change than the nuclei. Thus this approximation is violated whenever the electrons and nuclei have similar energy scale

²Thus the energies are expressed in Hartrees, $1 Ha = 27.2 \text{ eV}$ and distances in Bohr radii, $1 a_0 = 0.529 \text{ \AA}$

which is also referred to as an uncorrelated wave function. By using the variational principle the Schrodinger-like equation takes the following form [22],

$$\left[-\frac{1}{2}\nabla^2 + V(\mathbf{r}) + V_H(\mathbf{r}) \right] \phi_i(\mathbf{r}) = \epsilon_i \phi_i(\mathbf{r}) \quad (2.6)$$

ϵ_i are the energy eigenvalues. The first two terms have the same interpretation as in equation 2.2. The interaction term between the electrons is given by the Hartree potential $V_H(\mathbf{r})$

$$V_H(\mathbf{r}) = \int \frac{n(\mathbf{r}')}{|\mathbf{r} - \mathbf{r}'|} d\mathbf{r}' \quad (2.7)$$

where the electron density is expressed as

$$n(\mathbf{r}) = \sum_k \phi_k^*(\mathbf{r}) \phi_k(\mathbf{r}) \quad (2.8)$$

thus V_H is the average potential electron i experiences resulting from a charge density caused by all the other electrons. In the Hartree method all electrons occupy different states, but it clearly violates the antisymmetry principle 2.3. Notice that V_H contains a coupling between orbital i and itself, but clearly an electron does not interact with itself. This will be naturally accounted for in the Hartree-Fock method.

2.1.2 Hartree-Fock method

To take into account the exclusion principle for fermionic systems, Hartree-Fock method [23] introduces the Slater-determinant[24] for N-electron system

$$\Psi(\{\mathbf{r}_i\}) = \frac{1}{\sqrt{N!}} \begin{vmatrix} \phi_1(\mathbf{r}_1) & \phi_1(\mathbf{r}_2) & \dots & \phi_1(\mathbf{r}_N) \\ \phi_2(\mathbf{r}_1) & \phi_2(\mathbf{r}_2) & \dots & \phi_2(\mathbf{r}_N) \\ \vdots & \vdots & & \vdots \\ \phi_N(\mathbf{r}_1) & \phi_N(\mathbf{r}_2) & \dots & \phi_N(\mathbf{r}_N) \end{vmatrix} \quad (2.9)$$

Note that interchanging two rows in the determinant are equivalent to interchanging two single particle states. And two particles in the same position results in zero determinant. Similarly as for the Hartree method, using the variational principle the governing equation is,

$$\left[-\frac{1}{2}\nabla^2 + V(\mathbf{r}) + V_H(\mathbf{r}) + V_X(\mathbf{r}) \right] \phi_i(\mathbf{r}) = \epsilon_i \phi_i(\mathbf{r}) \quad (2.10)$$

The effect of the exchange interaction $V_X(\mathbf{r})$ is a direct consequence of the exclusion principle, hence no two electrons occupy the same eigenstate. Computationally the continuous

wave functions are approximated using a finite set of M basis functions $\chi_1(\mathbf{x}), \chi_2(\mathbf{x}), \dots, \chi_M(\mathbf{x})$ given by

$$\phi_j(\mathbf{x}) = \sum_{i=1}^M \alpha_{ji} \chi_i(\mathbf{x}) \quad (2.11)$$

where α are the expansion coefficient. The size of the basis set will affect the accuracy of the calculation and the computational cost. This is also referred to as to as formulation within the *linear combination of atomic orbitals* (LCAO), where χ_i is the atomic valence orbitals. Equation 2.10 is nonlinear with a circular nature, and thus solved iteratively, by the self-consistent field(SCF) method. The SCF method will be addressed in detail in section 2.5. Notice that the self-energy term in the Hartree energy is cancelled by the exchange contribution as result of the antisymmetry of the wave function. But the HF method still ignores the correlation between electrons.

2.2 The foundations of DFT

This section presents an alternative approach, in which the non trivial reformulation of the many-body problem by using the electron density as a key observable. Thus reducing the problem to quantities in the real 3-dimensional space. The formulation of DFT is derived from the Hohenberg-Kohn theorem[25].

Theorem . *An energy functional³ $E[n(\mathbf{r})]$ for interacting electrons within an external potential $V(\mathbf{r})$ can be uniquely⁴ defined by the electron density $n(\mathbf{r})$. Further the global minimum of the energy functional is the exact ground state energy of the system $E[n_0(\mathbf{r})]$ where $n_0(\mathbf{r})$ being the exact ground state density that minimizes this functional.*

2.3 The Kohn-Sham equations

The Hohenberg-Kohn theorem state that the total energy of the system can be written as a functional of the electron density $E[n]$. In the previous section the ground state was found by varying the energy with respect to the wave function. This is done in two stages, first minimizing a given electron density with respect to the wave functions and then minimize with respect to that density, written as

$$E[n] = \min_{\Psi \rightarrow n} \langle \Psi | H | \Psi \rangle \quad (2.12)$$

Since the exact form of this functional is still unknown, many approximations have been developed. The total energy of the system can be rewritten i terms of the universal functional $F[n]$,

³A functional assigns a number $F[f]$ to a function f .

⁴Uniquely means up to an arbitrary additive constant.

$$F[n] = \min_{\Psi \rightarrow n} \langle \Psi[n] | T_e + V_{ee} | \Psi[n] \rangle \quad (2.13)$$

Finally minimize over all N-electron densities $n(\mathbf{r})$,

$$E = \min_n \left\{ \int d\mathbf{r} n(\mathbf{r}) V(\mathbf{r}) + F[n] \right\} \quad (2.14)$$

The idea that makes the Kohn-Sham equations is to split this term into Coulombic -and kinetic energy of independent electrons, and extra term for the exchange correlation energy E_{XC} ,

$$E[n] = -\frac{1}{2} \sum_{i=1}^N \int d\mathbf{r} \phi_i^*(\mathbf{r}) \nabla^2 \phi_i(\mathbf{r}) + \int d\mathbf{r} n(\mathbf{r}) V(\mathbf{r}) + \frac{1}{2} \int \int d\mathbf{r} d\mathbf{r}' \frac{n(\mathbf{r})n(\mathbf{r}')}{|\mathbf{r} - \mathbf{r}'|} + E_{XC}[n(\mathbf{r})] \quad (2.15)$$

$$E[n] = T_e[n(\mathbf{r})] + V[n(\mathbf{r})] + V_H[n(\mathbf{r})] + E_{XC}[n(\mathbf{r})] \quad (2.16)$$

Hence the unknown(nontrivial) contribution is contained in the exchange correlation term. The remaining task is to determine the density. From the above theorem it is shown that the ground state density n_0 minimizes the total energy, which is also referred to as the Hohenberg-Kohn variational principle [26],

$$\left. \frac{\delta E[n]}{\delta n} \right|_{n_0} = 0 \quad (2.17)$$

Similarly as for the Hartree-Fock method the variational principle leads to the Kohn-Sham equations for the wave functions ϕ_i ,

$$\left[T_e(\mathbf{r}) + V(\mathbf{r}) + V_H(\mathbf{r}) + V_{XC}(\mathbf{r}) \right] \phi_i(\mathbf{r}) = \epsilon_i \phi_i(\mathbf{r}) \quad (2.18)$$

where the first three terms in the bracket are identical to those in the Hartree-Fock equations 2.10 and the exchange correlation potential $V_{XC}(\mathbf{r})$ is given by,

$$V_{XC}(\mathbf{r}) = \left. \frac{\delta E_{XC}[n]}{\delta n} \right|_{n(\mathbf{r})} \quad (2.19)$$

Thus all quantum effects are in E_{XC} . Even though the correlation energy is a relatively small fraction of the total energy of a solid, it contains most of the energy of the chemical bonding or atomization energy [27]. Hence accurate approximations of E_{XC} lies in the heart of the DFT method.

2.4 The exchange-correlation functional

This section introduces different approximations for the exchange-correlation functional. The simplest one is the *Local Density Approximation* LDA[28]. Where this functional is exactly known for the homogeneous electron gas. This system is closely related to the free electron gas [29], but also includes Coulomb repulsion between electrons,

$$E_{XC}^{LDA}[n(\mathbf{r})] = \int n(\mathbf{r})\epsilon_{XC}^{LDA}[n(\mathbf{r})]d\mathbf{r} \quad (2.20)$$

where $\epsilon_{XC}^{LDA}[n(\mathbf{r})]$ represents the exchange-correlation XC-energy per electron of a homogeneous electron gas with density $n(\mathbf{r})$. The XC-energy is split linearly in two terms, exchange $\epsilon_X^{LDA}[n]$ and correlation $\epsilon_C^{LDA}[n]$. The correlation term is estimated numerically by use of quantum Monte Carlo methods. The exchange term is derived exactly in this case

$$\epsilon_X^{LDA} = -\frac{3}{4} \frac{3^{1/3}}{\pi} n^{1/3}(\mathbf{r}) \quad (2.21)$$

More accurate exchange functionals includes also some derivatives of $n(\mathbf{r})$, which goes by the name *Generalized Gradient Approximation* GGA[30]. Different conventional GGA functionals tend to improve the total energy and atomization energy compared to LDA. These are PW91(Perdew-Wang 1991) [31], PBE(Perdew-Burke-Ernzerhof) [32]. The general GGA functional is given by

$$E_{XC}^{GGA}[n(\mathbf{r})] = \int f(n(\mathbf{r}), \nabla n(\mathbf{r}))d\mathbf{r} \quad (2.22)$$

where f is some function of $f(n(\mathbf{r}), \nabla n(\mathbf{r}))$. The functional is again divide into an exchange term E_X^{GGA} and correlation term E_C^{GGA} . The form of the correlation term depends on the functional, while the exchange term is

$$E_X^{GGA}[n] = \int n(\mathbf{r})\epsilon_X^{LDA}(n(\mathbf{r}))F_X^{GGA}(s)d\mathbf{r} \quad (2.23)$$

ϵ_X^{LDA} is the uniform exchange as in LDA, and $F_X^{GGA}(s)$ is an enhancement factor for local exchange [33], where s is a reduced dimensionless variable consisting of the electron density and its gradient. The conventional GGA exchange functionals differs in this enhancements factor[33].

2.5 Calculation scheme

The problem now remains to solve the Kohn-Sham equations, and hence obtain the ground-state energy. The governing equation written in a more convenient way are,

$$\left[-\frac{1}{2}\nabla^2 + V_{eff}(\mathbf{r}) \right] \phi_i(\mathbf{r}) = \epsilon_i \phi_i(\mathbf{r}) \quad (2.24)$$

where V_{eff} encapsulates the sum of $V(\mathbf{r})$, $V_H(\mathbf{r})$ and $V_{XC}(\mathbf{r})$.

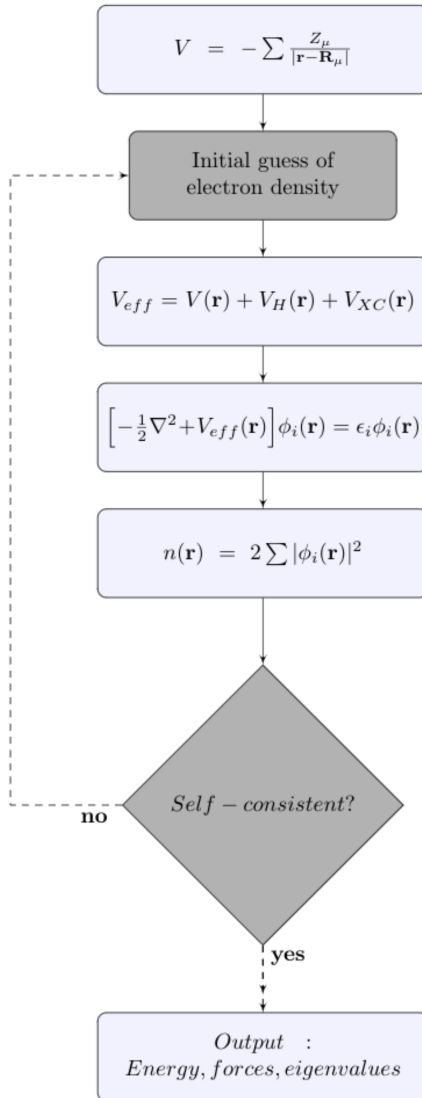


Figure 2.1: Flow-chart for solving the Kohn-Sham equations 2.18 in a self-consistent scheme. The loop terminates when the desired density and the previous density differ by less than a user defined tolerance, adapted from [2].

Equation 2.24 looks like the usual eigenvalue problem, but notice that to determine the eigenfunctions $\phi_i(\mathbf{r})$ and the energies ϵ_i the effective potential V_{eff} has to be known. The difficult part is that since both V_H and V_{XC} depends on the density, and the density depends again on the unknown eigenfunctions ϕ_i . The practical procedure for the self-consistent scheme is to determine the nuclear potential V , (the nuclear coordinates can be found from a crystallographic data or Hellmann-Feynman theorem, see section below) and start with an initial guess of the electron density and thus approximating V_H and V_{XC} , which determine the effective potential. New solutions are obtained by solving the Kohn-Sham equations, these are then used to construct a better density, and then used again as a trial density. This numerical solutions is done iteratively until the desired density and the previous density differ by less than a predetermined tolerance. The procedure is visualized in Figure 2.1. After obtaining the ground-state density the total energy of the system can be calculated.

2.6 Hellmann-Feynman forces

When the self-consistent scheme above reaches a minimum energy level for a given ionic configuration, forces exerted on ions can determined. These calculated forces can be used to determine a new ionic configuration, where a new electronic loop can be run. The analytical forces are obtained from the Hellmann-Feynman theorem [34]. Which states that for the minimum Kohn-Sham eigenstates, the forces exerted from electrons on an ion J is the partial derivative of the Kohn-Shame energy with respect to the ions position \mathbf{R}_J ,

$$\mathbf{F}_J^e = -\frac{\partial E}{\partial \mathbf{R}_J} \quad (2.25)$$

Also referred to as Hellmann-Feynman forces. Where this forces can be used to find the equilibrium geometries of a solid by varying \mathbf{R}_J until the energy is a minimum and Equation 2.25 is zero [27].

2.7 Dispersion correction

All functional introduced so far are either localized (LDA) or semi-localized (GGA) and thus does not account for long-range dispersion correction, especially for weak interaction for layered material like clay. Constant effort has been focused to develop functionals that model dispersion interactions. van der Waals density functional (vdW-DF) of Lundqvist et al [35, 36, 37]. And the method of Grimme termed as DFT-D3 and further revised to SCC-DFTB-D3(BJ) is employed in this work [18, 38]. This methods adds a dispersion term to the original Kohn-Sham energy E_{KS-DFT} , resulting in a total energy of

$$E_{DFT-D(3)} = E_{KS-DFT} + E_{disp} \quad (2.26)$$

where E_{disp} is the empirical fitted dispersion correction, in the following form [18],

$$E_{disp} = \sum_{AB} \dots \sum_{6,8,10,\dots} s_n \frac{C_{AB}^n}{r_{AB}^n} f_{d,n}(r_{AB}) \quad (2.27)$$

where s_n is the global scaling factors, $f_{d,n}$ is the damping function corresponds to the range of the dispersion correction and C_n^{AB} is the n -th order averaged dispersion coefficient for atom pair AB, with the distance r_{AB} between them. In the short range the D3(0) dispersion energy decay to zero, leading to artificial repulsive dispersion force for some cases, resulting in longer bond lengths. Since dispersion should always be attractive, the more reasonable behavior at short interatomic distances is introduced in D3(BJ)[38].

2.8 Computational approaches to DFT

This section discusses some key concepts in simplification and modelling of DFT based computation.

2.8.1 Reciprocal space and Bloch's theorem

For a crystal structure, a periodic potential is assumed. By Bloch's theorem [29] the eigenfunctions of ψ are expressed by the product of a plane wave and a periodic function $u_k(\mathbf{r})$ with periodicity matching the periodic potential, the Bloch functions is given by,

$$\psi_k(\mathbf{r}) = e^{i\mathbf{k}\cdot\mathbf{r}}u_k(\mathbf{r}) \quad (2.28)$$

Further the reciprocal lattice vector is $\mathbf{G} = m_1\mathbf{b}_1 + m_2\mathbf{b}_2 + m_3\mathbf{b}_3$, where the lattice vectors defines the unit cell in reciprocal space, the *Brillouin zone* (BZ). Related to the real space lattice vectors by [29]

$$\mathbf{b}_1 = 2\pi \frac{\mathbf{a}_2 \times \mathbf{a}_3}{\mathbf{a}_1 \cdot (\mathbf{a}_2 \times \mathbf{a}_3)}, \quad \mathbf{b}_2 = 2\pi \frac{\mathbf{a}_3 \times \mathbf{a}_1}{\mathbf{a}_2 \cdot (\mathbf{a}_3 \times \mathbf{a}_1)}, \quad \mathbf{b}_3 = 2\pi \frac{\mathbf{a}_1 \times \mathbf{a}_2}{\mathbf{a}_3 \cdot (\mathbf{a}_1 \times \mathbf{a}_2)} \quad (2.29)$$

thus $\mathbf{a}_i \cdot \mathbf{b}_j = 2\pi\delta_{ij}$, where δ_{ij} is the Kronecker-delta, such that $\mathbf{G} \cdot \mathbf{a}_i = 2\pi m_i$. Hence longer real space vectors yields shorter lattice vectors in reciprocal space. All information are contained in the first Brillouin zone, and thus infinite crystalline material can be represented by finite numbers of wave functions. Exploiting further symmetry the evaluation of the integrals can be further reduced to the *irreducible Brillouin zone*(IBZ), for further detailed explanation see [2].

2.8.2 k-point sampling

A corollary of Bloch theorem is that all information is contained in the first Brillouin zone (BZ). That means all unique \mathbf{k} vector are found in this zone, and for a given \mathbf{k} vector outside this zone can always be translated back to the first BZ by an appropriate choice of reciprocal vector \mathbf{G} . Thus the governing equations are solved for wavevectors in the first BZ. Numerically this is done by discretizing the \mathbf{k} -space and finding solution of the wavefunctions at these mesh points. Accurate results demands more k -point, and hence longer computational time. See for instance the general method proposed by Monkhorst and Pack [39].

2.8.3 Convergence

Although density functional calculations follows directly from solving the many-electron problem then mapped to Kohn-Sham equations, the practical procedure depends on a number of computational parameters which governs the precision of the results. Two important parameters are the number of basis functions used to expand the Kohn-Sham orbitals and the k-point mesh used over the Brillouin zone. Hence a test convergence of the results should be checked with respect to these computational parameters.

2.9 Potential energy surface

The potential energy surface captures the idea that each structure or configuration has associated with it a unique energy landscape. Thus a nonlinear molecule consisting of N atoms has $3N-6$ independent coordinates [29]. From the curvature of this energy landscape stationary points can be classified, given by the second derivative of the energy with respect to each coordinate, contained by the *Hessian matrix* \mathbf{H} ,

$$\mathbf{H} = \begin{pmatrix} \frac{\partial^2 E}{\partial x_1^2} & \frac{\partial^2 E}{\partial x_1 \partial y_1} & \cdots & \frac{\partial^2 E}{\partial x_1 \partial z_N} \\ \vdots & \vdots & \ddots & \vdots \\ \frac{\partial^2 E}{\partial z_N \partial x_1} & \frac{\partial^2 E}{\partial z_N \partial y_1} & \cdots & \frac{\partial^2 E}{\partial z_N^2} \end{pmatrix} \quad (2.30)$$

where stationary points are given by non-negative Hessian, and physically stable states corresponds to the minima in the energy landscape. Hence the minimum energy path has the smallest energy change. Between two minima **A** and **B**, the energy path passes through a first order saddle point, referred to as the *transition state* (**TS**), where the Hessian has exactly one negative value in this state. Thus the *activation energy* (E_a) in crossing this energy barrier is,

$$E_a = E(\mathbf{TS}) - E(\mathbf{B}) \quad (2.31)$$

The eigenvectors \mathbf{e} of the Hessian satisfy the $\mathbf{H}\mathbf{e} = \lambda\mathbf{e}$, where λ are the corresponding eigenvalues, where the vibrational frequency is

$$\nu_i = \frac{1}{2\pi} \sqrt{\frac{\lambda_i}{m}} \quad (2.32)$$

representing the normal modes of vibration. Equation 2.32 show the case where the transition state with negative eigenvalue yield an imaginary frequency.

2.10 Review of SCC-DFTB

Density functional based tight-binding (DFTB) is an approximation method based on the Kohn-Sham (KS) approach to density functional theory. In contrast to DFT this approach is not a first principle, and in all flavors of DFTB a significant work of parametrization must be done. Although this method have shown reasonable accuracy in structure and reaction

energies of organic and bioorganic molecules [17], the formulation of the total energy is still one of the big challenges in the DFTB parametrization. Based on this method, the total energy is divided in two contributions

$$E = E_e + E_{rep} \quad (2.33)$$

where E_e is the electronic energy and E_{rep} is the repulsion energy. The total electron density ρ is given by

$$\rho(\mathbf{r}) = \rho_0(\mathbf{r}) + \Delta\rho(\mathbf{r}) \quad (2.34)$$

where ρ_0 is the reference density, perturbed by $\Delta\rho(\mathbf{r})$. The XC-functionals are then Taylor expanded up to second order,

$$E_{XC}[\rho_0 + \Delta\rho] = E_{XC}[\rho_0] + \int \frac{\delta E_{XC}}{\delta\rho_0} \Delta\rho d\mathbf{r} + \frac{1}{2} \int \int \frac{\delta^2 E_{XC}}{\delta\rho'_0 \delta\rho_0} \Delta\rho' \Delta\rho d\mathbf{r}' d\mathbf{r} \quad (2.35)$$

Using Equation 2.33 and 2.34, the KS density functional reads,

$$\begin{aligned} E_{XC}[\rho_0 + \Delta\rho] &= \sum_i^N \langle \psi_i | H^0 | \psi_i \rangle \\ &+ \frac{1}{2} \int \int \left(\frac{1}{|\mathbf{r} - \mathbf{r}'|} + \frac{\delta^2 E_{XC}}{\delta\rho'_0 \delta\rho_0} \right) \Delta\rho' \Delta\rho d\mathbf{r}' d\mathbf{r} \\ &- \frac{1}{2} \int \int \frac{\rho_0 \rho'_0}{|\mathbf{r} - \mathbf{r}'|} d\mathbf{r}' d\mathbf{r} + E_{XC}[\rho_0] - \int V_{XC} \rho_0 \mathbf{r} + E_{nn} \end{aligned} \quad (2.36)$$

which correspond to three energy contributions, the first term on the right is the electronic energy E_0 , the second term is the charge fluctuation correction to electronic energy E_{SCC} and last term is the repulsion energy E_{rep} . E_{rep} is the practical equivalent as XC-functional in DFT, where it contains all nontrivial terms, and hence approximated by simple functions. Take the case with the Hartree term,

$$-\frac{1}{2} \int \int \frac{\rho_0 \rho'_0}{|\mathbf{r} - \mathbf{r}'|} d\mathbf{r}' d\mathbf{r}$$

and divided into atomic volumes, the integral becomes a sum over atom pairs, and each term depends only on the atomic numbers given by their valence number Z_I^v , and their distance apart,

$$\frac{Z_I^v Z_J^v}{|\mathbf{R}_I - \mathbf{R}_J|} = \frac{Z_I^v Z_J^v}{R_{IJ}} \quad (2.37)$$

In similar fashion, the repulsive energy is approximated as

$$E_{rep} = \sum_I V_{rep}^{IJ}(R_{IJ}) \quad (2.38)$$

the repulsive function $V_{rep}^{IJ}(R)$ is given to each pair of atoms IJ depending only on the atomic numbers. Notice also the on-site contributions contained in E_{rep} , resulting only in a shift of the total energy by a constant. The pair repulsive functions $V_{rep}^{IJ}(R)$ are obtained by DFT fitting, or in the simulation of this work, experimental based parametrization, given by the QUASINANO2015 parameter set [40].

Computational details

All calculations in this present work were implemented using first-principle calculations based on DFT and semiempirical method DFTB based on Tight-Binding Hamiltonian. Implemented by the Amsterdam Modelling Suite (AMS) program [41]. ADF modelling in the Kohn-Sham approach uses Slater-Type Orbitals (STOs) together with Numerical Atomic Orbitals (NAOs) as basis sets(ref). Due to time consumption of Full DFT calculation for a bulk structure in ADF, all calculation of the fluorohectorite structures are done using SCC-DFTB.

3.1 Geometry optimization

All simple non-periodic calculation of the cation-water complexes was done using ADF with STOs of the form

$$f(\mathbf{r}) = R_{nl}Y_{lm}(\theta, \phi) \quad (3.1)$$

R_{nl} is the radial part, where n is the principal quantum number, and l the angular momentum quantum number. $Y_{lm}(\theta, \phi)$ is the spherical harmonics, m is the magnetic quantum number. Notice the similarity to the solution of hydrogen-like atom, with smooth radial confinement given by Fermi-Dirac function [42]. The ADF database comes with a range of basis sets according to computational accuracy. The minimal basis set is SZ(single zeta) with only one function for each atomic orbital [33]. Followed by DZ(double zeta) with two basis function for each atomic orbital. Polarized orbital state could also be specified. Triple zeta with one polarization(TZP) function was employed in the calculations. Further the basis sets is complemented by "Frozen core" approximation of the inner electron shells of the atoms, with the following options Large-Medium-Small. For these small systems of atoms the option "small" was chosen. A given "Numerical quality" key with the options Basic-Normal-Good-Very good-Excellent will determine the numerical quality for several aspects of the calculations. Given by the Becke grid, k -space integration, Zlm Fit and Soft Confinement. Becke grid is the numerical integration grid [43]. The k -space integra-

tion determines the number of k -points specified in each direction for the geometry of the unitcell. The following unique k -points are assigned to each key, "Good" = 13 points and "Normal" = 5 points. The calculations in this work are set to "Good". Zlm Fit is the electron density fitting scheme into atomic densities approximated by radial spline functions and real spherical harmonics(Zlm).

The code also supports variable periodicity given by the following dimensions 0D-none, 1D-chain, 2D-slab and 3D-bulk geometries. For the simple cation-water complexes the the periodicity was sat to none. While for the fluorohectorite structure all calculation was given for a bulk geometry at the level of SCC-DFTB.

The exchange correlation(XC) functional chosen was the revised Perdew-Burke-Ernzerhof (revPBE), within the generalized gradient approximation. Other XC functional are also tested for comparison, see section 4.1. All calculation are geometry optimized to find a self-consistent energy minimum, with a user specified convergence criteria. The default values are, energy changes 0.001 Hartree for the next iteration of the geometry. And 0.001 Hartree/Angstrom for nuclear gradients, 0.01 Angstrom for changes in bond length and 0.5 degrees for changes in bond-and dihedral angles.

For the calculations of the bulk fluorohectorite structure the *self-consistent density functional tight binding* SCC-DFTB was used, with the QUASINANO2015(QN15) paramter set, [17, 18]. This method only supports the elements H-Ca [40]. For the purpose of investigating the swelling constant a full lattice optimization was chosen. This computational expensive task is show to be in order 2-3 faster than conventional DFT lattice optimization [40]. It is worth mentioning that due to DFTB fitting procedures and the repulsive potential, DFTB calculations is harder to reproduce compared to the conventional and well documented XC-functionals.

3.1.1 Fast Inertial Relaxation Engine

Finding the nearest atomic structure with the minimum potential energy from a given initial configuration is the heart of every common tasks in computational material science. The Fast Inertial Relaxation Engine(FIRE) used in DFT and DFTB for large numbers of atoms [41, 44]. This molecular dynamics scheme keeps up easiley with the conventional schemes like steepest decent, conjugate gradient(CG), Broyden-Fletcher-Goldfarb-Shanno(L-BFGS). Contrary to the conventional schemes the FIRE algorithm relies on inertia, illustrated by the following case: Given a hiker in a dense forrest searching for the fastest way back to the bottom of a valley with energy landscape $E(\mathbf{x})$. The FIRE algorithm will recommend the hiker to follow the equation

$$\dot{\mathbf{v}} = \mathbf{F}(t)/m - \gamma(t)|\mathbf{v}(t)|(\hat{\mathbf{v}}(t) - \hat{\mathbf{F}}(t)) \quad (3.2)$$

with mass m , velocity \mathbf{v} and the force $\mathbf{F} = -\nabla E(\mathbf{x})$, with the hat as a unit vector. The hiker is now recommended to accelerate in direction steeper than the current direction of motion guided by the function $\gamma(t)$ if the power $P(t) = \mathbf{F}(t) \cdot \mathbf{v}(t)$ is positive, otherwise stop for uphill motion, $\gamma(t)$ should also be restricted for not to large values [44].

3.2 Mulliken charge analysis

The atomic partial charges was estimated at the level of DFT and SCC-DFTB using *Mulliken population analysis*. The main idea behind this method is to expand the atomic orbitals in basis functions defining the the total density matrix. Then the charge of each basis functions of the given atom is assigned to that atom [45]. Notice other partitioning method like Hirshfeld or Voronoi will give other results, since there is no operator corresponding to the atomic charge.

3.3 Bader charge analysis

The other method of partitioning the continuous electronic charge density is given by *Bader charge analysis* [46], and was run to determine the charge transfer between the interlayer cations and the hexagonal cavity at the surface of fluorohectorite. This method divides region into subsystems, usually contains one atom. The subsystems are separated by zero-flux surfaces, $\nabla n(\mathbf{r}) \cdot \hat{n} = 0$, where \hat{n} is the unit vector normal to the surface.

Results and Discussion

This section presents the results obtained during this work. This chapter is presented in two main sections. First considering a comprehensive study of the cation-water complex formation. Thereafter introducing the cation-water complex within the fluorohectorite interlayer to investigate the microscopic behavior of swelling as the water contents is increased.

4.1 Testing functionals

To determine whether a functional will achieve satisfactory results, several XC-functionals LDA, PW91, PBE, revPBE and revPBE-D3 were tested and compared. The latter functional includes dispersion correction. The bonding energy were calculated for the cation-water complex $M^{n+}(H_2O)_m$. Where the charge of the cation is $n = 1, 2$ and the number of water molecules $m = 1, \dots, 6$, thus

$$E_{bond} = E(M^{n+}(H_2O)_m) - (E(H_2O) + E(M^{n+}(H_2O)_{m-1})) \quad (4.1)$$

Figure 4.1 shows the the calculated bonding energy for $Li^+(H_2O)$. The curve of PW91, PBE and revPBE-D3 coincide with small difference of ~ 0.05 eV. Whereas the revPBE on average of 0.10eV show higher energies than PBE. Further the LDA functional systematically underestimates the energies of about 0.2eV compared to PBE. The M-O bond length is also important to investigate for the cation-water interaction, see Table 4.1. For these simple interaction the dispersion correction will not be included. It is further shown that revPBE improves the atomic total energies of PBE by a factor of 10 and a reduced mean absolute error from 8.1 to 4.9 kcal/mol [42]. Thus for accuracy with no more added computational cost the revPBE is chosen for further calculations. For the given cations with noble-gas like electron configuration all calculations were run spin restricted, hence spin effects will not be considered.

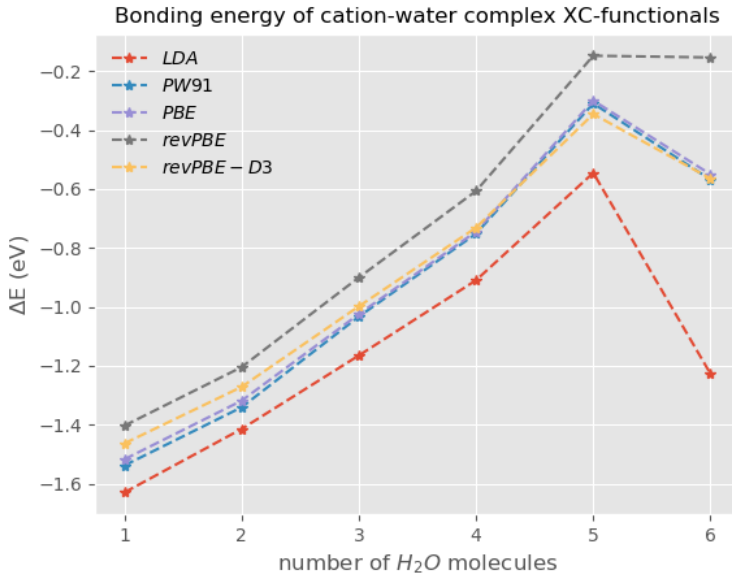


Figure 4.1: Bonding energy comparison of $\text{Li}^+(\text{H}_2\text{O})$ complex for the LDA, PW91, PBE, revPBE and revPBE-D3 XC-functionals. The latter functional include dispersion correction D3.

R_{M-O} (Å)	LDA	PW91	PBE	revPBE	revPBE-D3	SCC-DFTB	GFN1-xTB
Li^+	1.79	1.85	1.83	1.85	1.85	1.60	1.72
Na^+	2.16	2.28	2.23	2.28	2.30	2.35	2.08
K^+	2.52	2.62	2.63	2.68	2.73	2.65	2.48
Be^{2+}	1.47	1.48	1.48	1.49	1.49	1.38	1.45
Mg^{2+}	2.17	2.26	2.26	2.25	2.27	1.97	2.25
Ca^{2+}	2.25	2.33	2.34	2.24	2.38	2.68	2.03

Table 4.1: Calculated M-O distance for different methods.

4.2 Hydrated cations

4.2.1 Geometrical parameters

The geometrical parameters of the $M^{n+}(H_2O)$ was determined at the levels of DFT-revPBE and the tight-binding methods SCC-DFTB and GFN1-xTB. By examining the M-O distance and the H-O-H angle variation for the size and the charge of the cations. Figure 4.2 show clearly that increasing the cation size tend to increase the M-O distance. While the the M-O distance decreases when increasing the charge. These methods predicts the same trends with small discrepancy, except for Ca^{2+} calculated with SCC-DFTB, wich is about $\sim 0.4\text{\AA}$ larger than DFT-revPBE. The variation of H-O-H angle in the $M^{n+}(H_2O)$ complex compared to the isolated water molecule is given in Figure 4.3. The DFT-revPBE predicts that upon increasing the cation size the angle gets smaller, except for K^+ . And increasing the charge has the opposite effect, the angle increases. The SCC-DFTB shows the same trend as DFT-revPBE for the divalent cations, but the opposite effect for monovalent cations. The GFN1-xTB predicts a decreasing angle both for the variation of the size and charge.

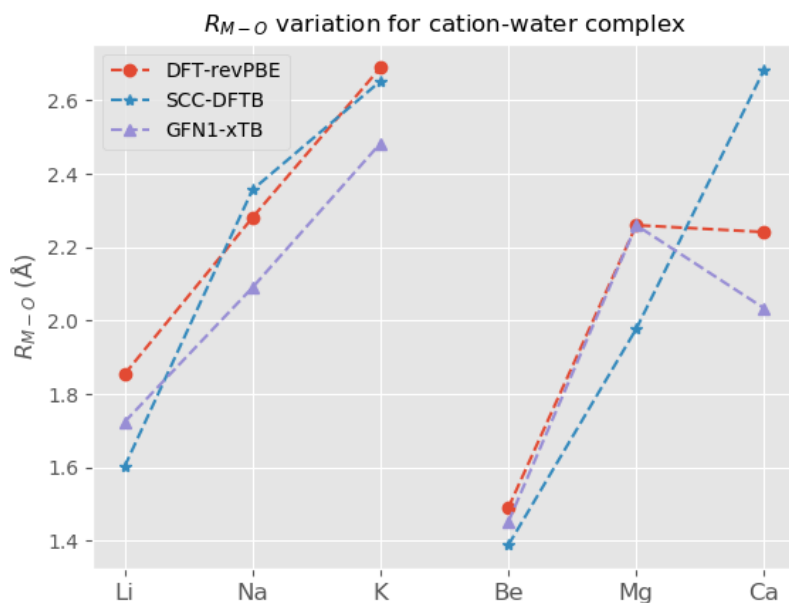


Figure 4.2: The M-O distance variation with charge and size for the mono-hydrated cation, using DFT-revPBE and the two tight-binding methods SCC-DFTB and GFN1-xTB.

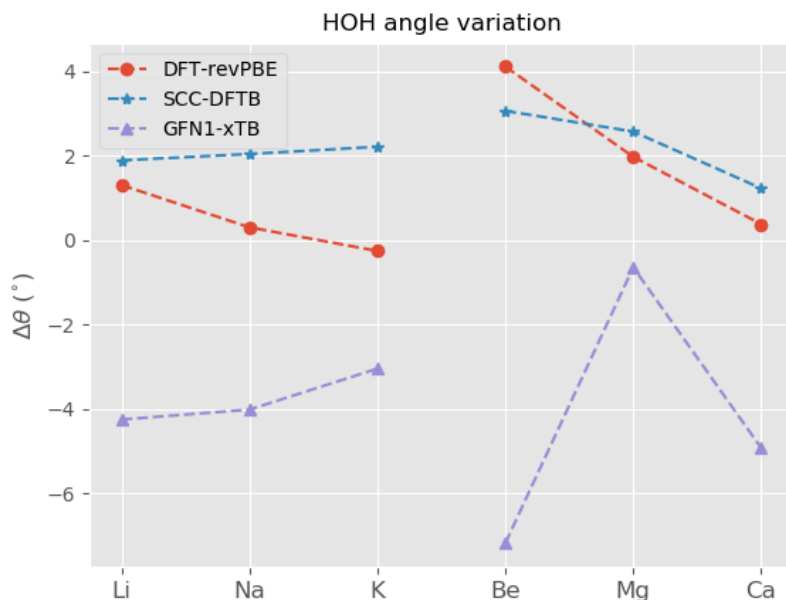


Figure 4.3: The H-O-H angle variation with charge and size for the monohydrated cation compared to the isolated H_2O molecule, using DFT-revPBE and the two tight-binding methods SCC-DFTB and GFN1-xTB.

The polarization of the cation clearly dictates the geometry of the complex. Which is also observed between the correlation of the M-O distance and ionic radius from Table 4.1. Where larger ionic radius results in larger M-O distance, consistent with previous study [47]. Calculating the atomic charges using Mulliken population analysis. Observing from Figure 4.5 the change in the electronic density from the single water molecule to the formation of the complex. The cation induces a shift in the electronic density towards the oxygen atom, making it more negative. Thus increasing the repulsion of the bonding electrons leading to a larger H-O-H angle. Furthermore leading to a significantly larger decrease (more positive) in the electronic charge on the hydrogen atoms. This shift effect the O-H bond distance, seen from Table 4.2 and 4.3. The deformation of the electronic cloud is also observed in the change of the shape of the highest occupied molecular orbital (HOMO), clearly observed for Be^{2+} Figure 4.4.

The geometry of the complex for $m = 2, \dots, 6$ is shown in Figure 4.5 with their respective geometry. For two water molecules the complex is linear for all cations except Ca^{2+} with $\angle\text{O-Ca-O} = 120.8$. And for three and four water molecules the complex is planar and tetrahedral respectively. Notice the hydration number for Be^{2+} is 4, thus for five water molecules the extra water molecule is in the second solvation shell connected with an hydrogen bond, see Figure 4.5. For the other cations the complex forms a square pyramidal for 5 water molecules. And as expected the cation-water complex with six water molecules is an octahedral. The hydration number are here defined to be the nearest-neighbor coordination between the cation and water molecules. The values are summarized in Table 4.4 with the experimental value in the parentheses given by [1].

Complex	$M^{n+}(\text{e})$	O (e)	H (e)	O-H (Å)
H_2O	-	-0.673	0.337	0.97
$\text{Li}^+(\text{H}_2\text{O})$	0.886	-0.656	0.385	0.99
$\text{Na}^+(\text{H}_2\text{O})$	0.949	-0.734	0.392	0.98
$\text{K}^+(\text{H}_2\text{O})$	0.970	-0.750	0.390	0.98
$\text{Be}^{2+}(\text{H}_2\text{O})$	1.531	-0.444	0.456	1.00
$\text{Mg}^{2+}(\text{H}_2\text{O})$	1.789	-0.699	0.455	0.99
$\text{Ca}^{2+}(\text{H}_2\text{O})$	1.820	-0.727	0.454	0.99

Table 4.2: Mulliken charge analysis for the monohydrated cations compared with the single water molecule. And the effect on the O-H distance. Calculated at the DFT level.

Complex	$M^{n+}(\text{e})$	O (e)	H (e)	O-H (Å)
H_2O	-	-0.433	0.216	1.02
$\text{Li}^+(\text{H}_2\text{O})$	0.644	-0.190	0.273	1.01
$\text{Na}^+(\text{H}_2\text{O})$	0.802	-0.322	0.260	1.02
$\text{K}^+(\text{H}_2\text{O})$	0.801	-0.312	0.255	1.02
$\text{Be}^{2+}(\text{H}_2\text{O})$	1.346	-0.127	0.390	1.04
$\text{Mg}^{2+}(\text{H}_2\text{O})$	1.632	-0.293	0.330	1.03
$\text{Ca}^{2+}(\text{H}_2\text{O})$	1.776	-0.353	0.288	1.03

Table 4.3: Mulliken charge analysis for the monohydrated cations compared with the single water molecule. And the effect on the O-H distance. Calculated at the SCC-DFTB level.

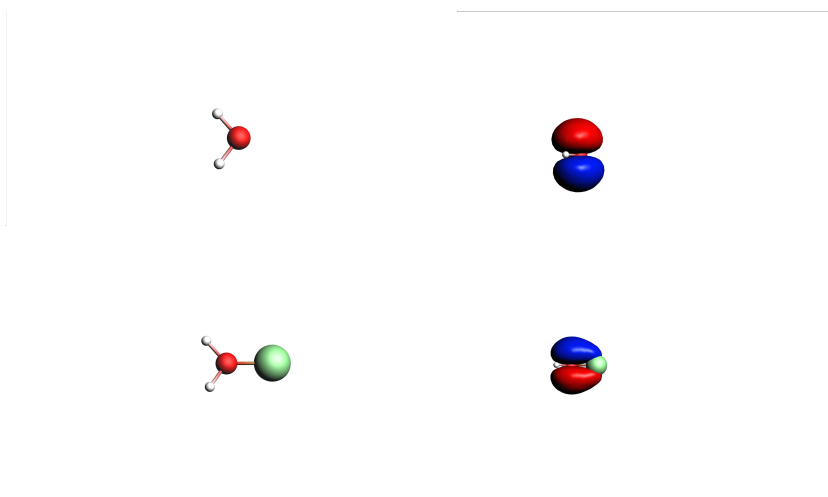


Figure 4.4: The displacement of the electron density depicted by the change in the HOMO orbital. The upper row is the HOMO for the single water molecule and the lower row is for Be²⁺(H₂O).

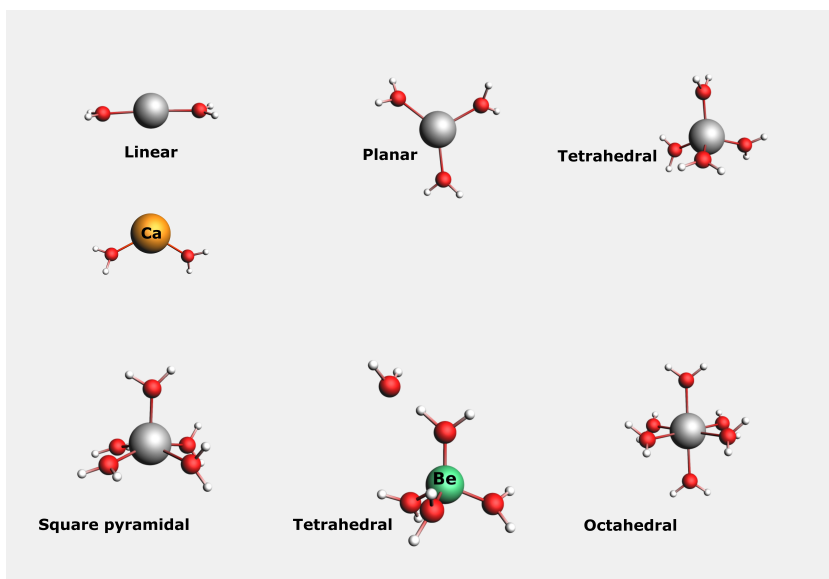
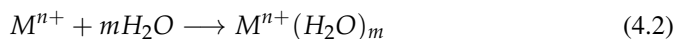


Figure 4.5: Configurations of the hydrated Li⁺-complex, and the special case for Be(H₂O)₅²⁺ and Ca(H₂O)₂²⁺. The geometry of the configuration is indicated underneath.

4.2.2 Bonding energy of cation-water complex

The energies of the interaction between the cation and several water molecules is important to understand the most probable configuration of the cation-water complex. Considering only coordination of the water molecules to the first hydration shell. Thus using a coordination number of 6 for the different cations. Notice due to bonding energy and geometry consideration this may vary for the different cations¹. See specially the case for Be^{2+} Table 4.4. The reaction taking place is



Using Equation 4.1 to calculate the bonding energy. The corresponding experimental quantity is referred to as the hydration enthalpy $\Delta_{hyd}H_{298}^\circ$, and as expected is an exothermic reaction, Table 4.9. The calculated bonding energy of the successive adding of water molecules to the cations is depicted in Figure 4.7 for the two different methods. From the DFT-revPBE it is observed that the ΔE increases with the size of the cation independently of the charge. Furthermore ΔE decreases with increased charge. SCC-DFTB predicts the same trends with the exception that the Li^+ -complex have higher binding energy than Ca^{2+} -complex, and further that hydration number 5 for Li^+ is energetically not favourable. the correlation between the methods are depicted in Figure 4.6, resulting in an average correlation coefficient $r = 0.89$.

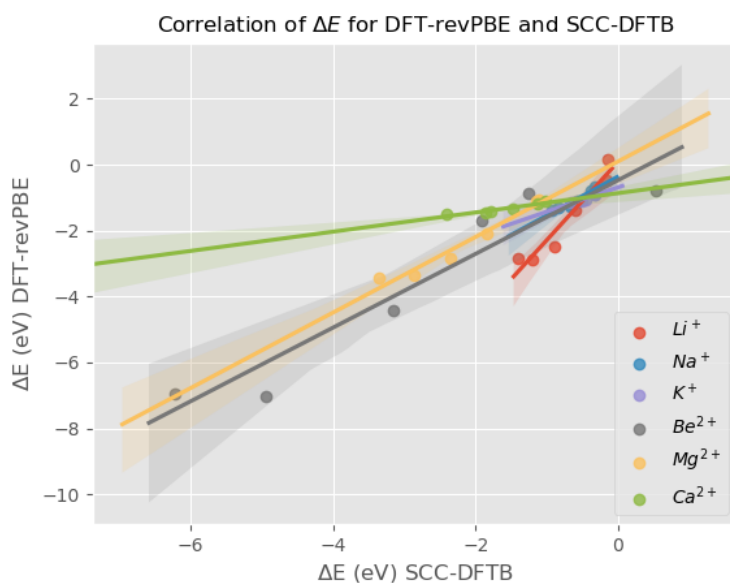


Figure 4.6: Correlation of the bonding energy for the cation-complex given by DFT and SCC-DFTB.

¹It depend also on the method used and the way the first hydration shell is defined.

Both methods predicts rather high binding energy for Be^{2+} , which is unexpected if extrapolating from the divalent cations Mg^{2+} and Ca^{2+} . From Table 4.1 the ionic radius of Be^{2+} is 0.34Å which gives Be^{2+} the charge to radius ratio (Z/r) of 6.45 [1] hence leading to a strong electrostatic ordering. Notice from Figure 4.7 that the process of progressive hydration of the cation liberates less energy for each added water molecule, hence less exothermic for each stage. Taking this point to account and the geometry consideration for each new water molecule, leading to a saturation of the solvation shell for each cation, given by the hydration number see Table 4.4, where the experimental values for the hydration number is given in parentheses. From a classical picture, the cation-water complex are described by the charge-dipole interaction. From Figure 4.8 ΔE correlates with $1/R_{M-O}^2$ for the charge of the cation and thus the interaction is purely electrostatic in nature, which is expected for the given cations with noble-gas like electron configuration. Thus ΔE and M-O bond length relationship is shown to be inversely linearly dependent, according to $E = A(1/R_{M-O}) + B$ where A and B are constants. Common ionic properties associated with clay interaction are summarized in Table 4.4 and Figure 4.9. Figure 4.9 summarizes the key concept underlying the microscopic behavior clay swelling discussed in next section.

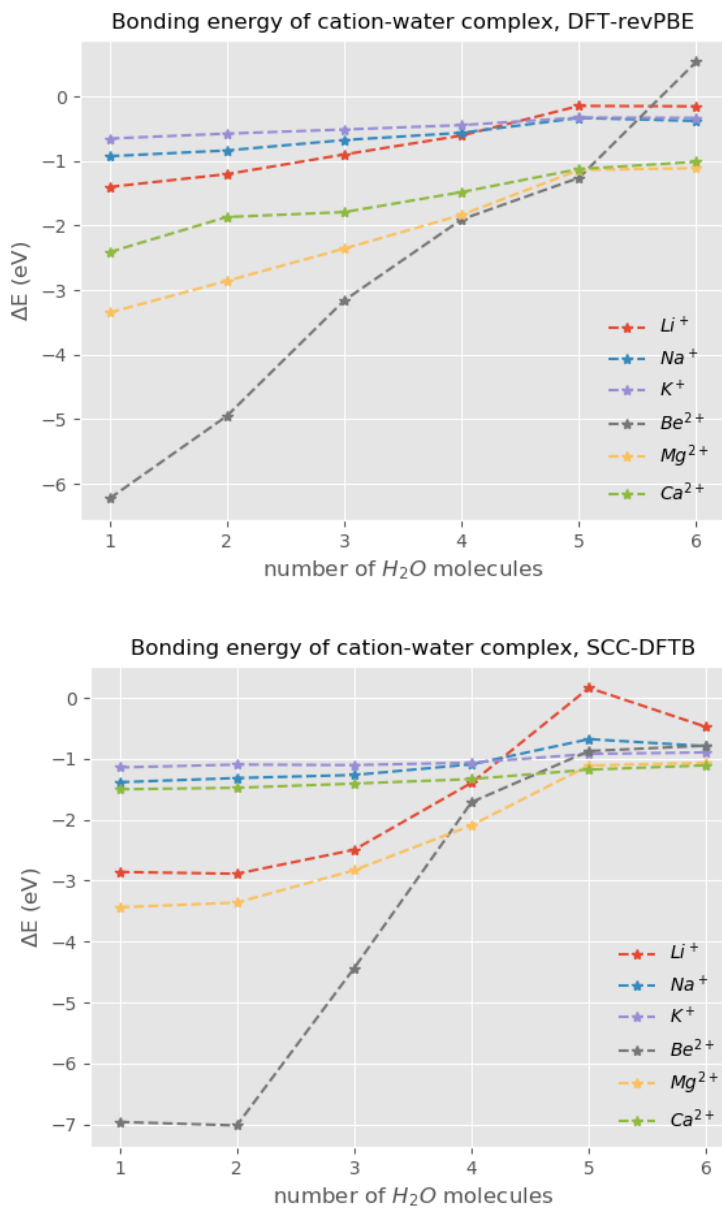


Figure 4.7: Bonding energy of cation-water complex using DFT-revPBE (upper graph) and SCC-DFTB (lower figure), showing the trends when changing the size and charge of the cation.

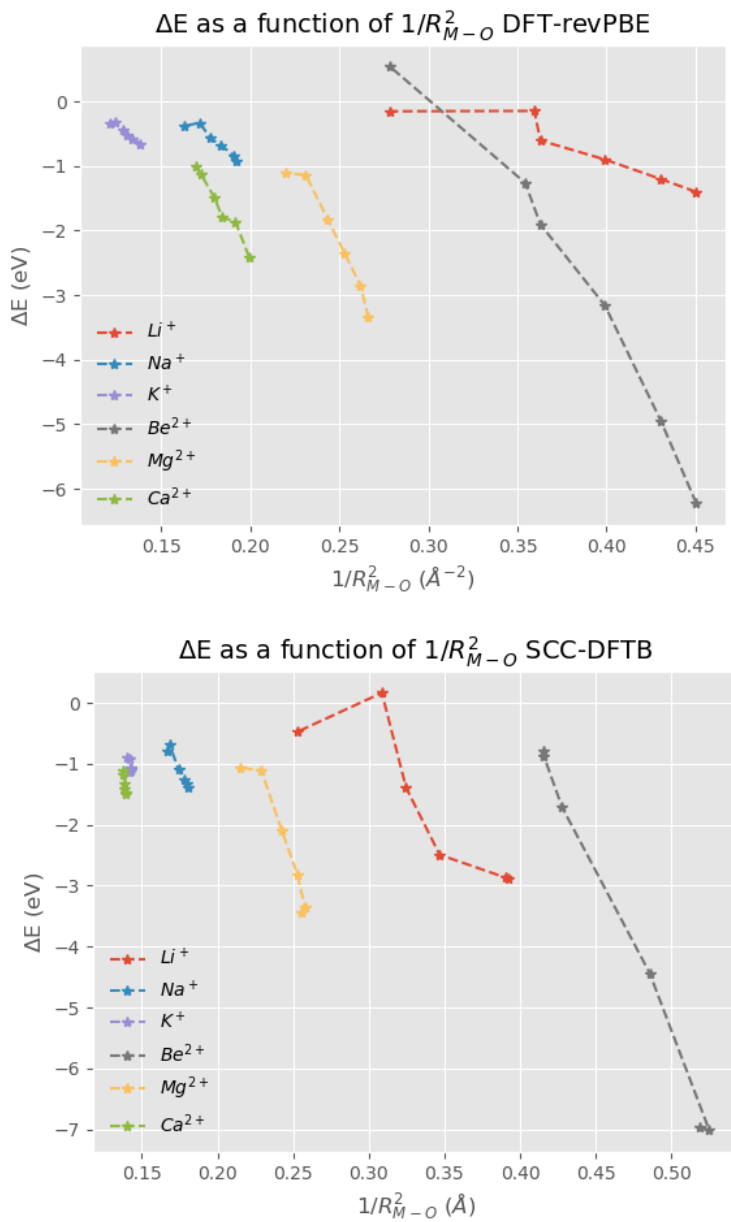


Figure 4.8: Correlation of the bonding energy and square of the reciprocal M-O distance for the cation-complex given by DFT(upper graph) and SCC-DFTB(lower graph).

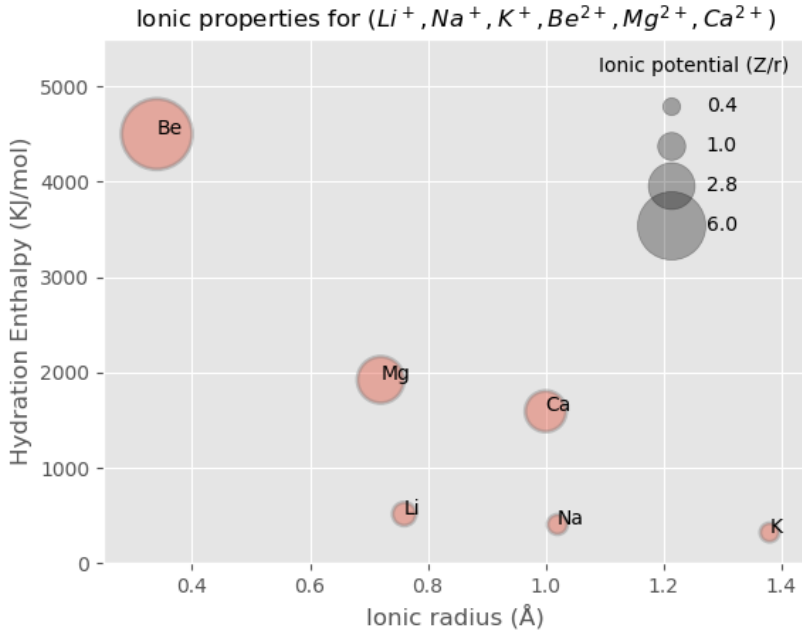


Figure 4.9: Cation properties associated with clay interaction, experimental values are given in [1].

Complex	Ionic radius (Å)	Ionic potential	Hydration enthalpy (kJ/mol)	Hydration number
Li^+	0.76	0.7	-515	6(5)
Na^+	1.02	0.5	-405	6(4)
K^+	1.38	0.45	-321	5(3)
Be^{2+}	0.34	6.45	-4560	4(4)
Mg^{2+}	0.72	2.8	-1922	6(6)
Ca^{2+}	1.00	2.15	-1592	6(6)

Table 4.4: Common experimental values of ionic properties associated with clay interaction, given in [1]. Experimental hydration number are given in parentheses.

4.3 Structure of hydrated Fluorohectorite

Introducing now the 2:1 clay structure of fluorohectorite (Fh). All calculation are done with the isomorphous substitution of Mg^{2+} in the octahedral sheet with Li^+ and the hypothetical case Na^+ . Hence the clay structure will now be abbreviated as Fh_{Li} or Fh_{Na}^2 . In the case for the divalent cations two Mg^{2+} were substituted with two- Li^+ or Na^+ . Notice that Na^+/Mg^{2+} substitution is not observed experimentally, but it yields further understanding of energetics and structural dynamics. The start geometry is such that the cations are hydrated by the water molecules confined in one plane for the case one water layer(1WL) and in two planes of the case of two water layers(2WL), depicted in Figures 4.10,4.11 and 4.12 for the case of dry, 1WL and 2WL respectively, of $Na-Fh_{Li}$. The left structures shows the unit cell in xz -plane while the right structure depicts the repeated unit cell in the xy -plane. Following the work by Kalo et al [13] the H_2O/Na molar ration was 3.2 and 5.6 for 1WL and 2WL respectively. To investigate effects beyond the first solvation shell, the calculation were done up to 4 water molecules for the 1WL case and 8 water molecules for the case of 2WL. Which is also consistent with other simulation and experimental work [48, 49].

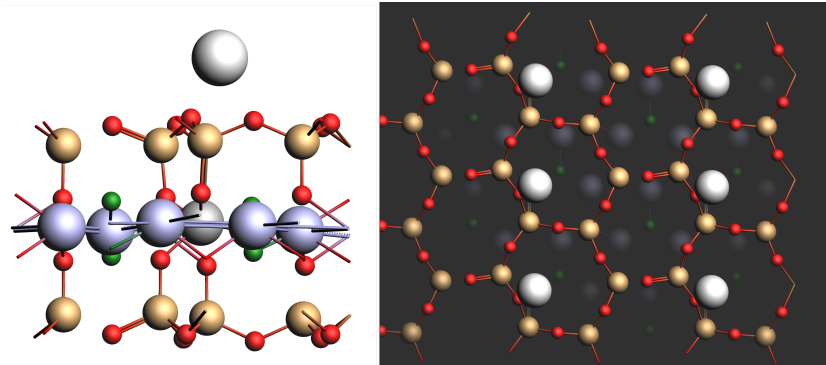


Figure 4.10: Snapshots of the simulated dry $Na-Fh_{Li}$, viewed from xz -plane in the left structure and the repeated unit cell in the right, viewed from the xy -plane.

²This should not be confused by the the interlayer cations Li^+ and Na^+

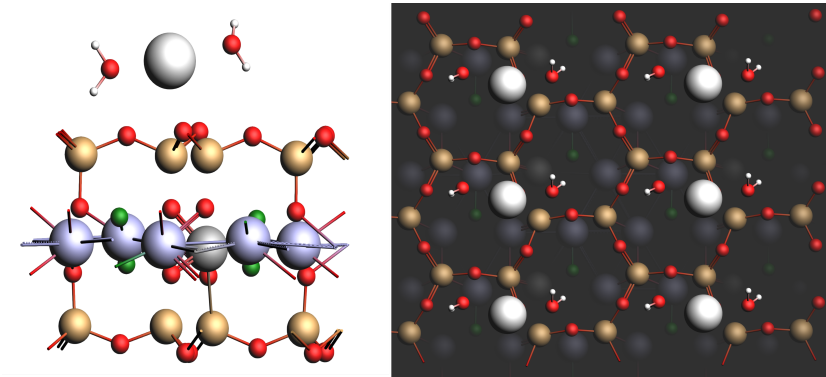


Figure 4.11: Snapshots of the simulated 1WL Na-Fh_{Li}, viewed from xz-plane in the left structure and the repeated unit cell in the right, viewed from the xy-plane.

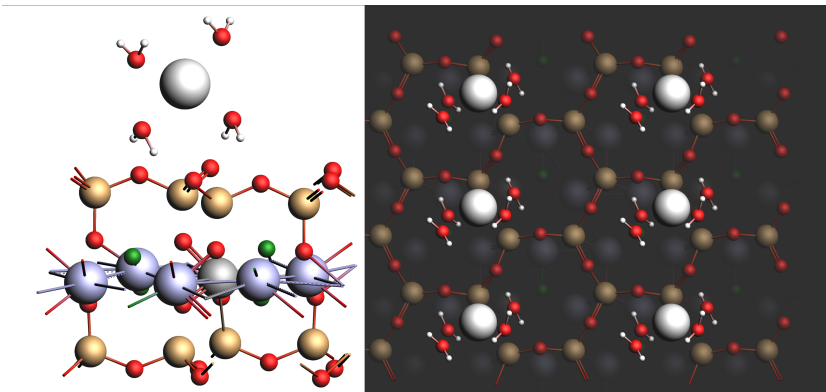


Figure 4.12: Snapshots of the simulated 2WL Na-Fh_{Li}, viewed from xz-plane in the left structure and the repeated unit cell in the right, viewed from the xy-plane.

For the optimized cell parameters of the pure Fh structure, $|b| = 9.63 \text{ \AA}$, and $|a| = 5.55 \text{ \AA}$ within 5% of experimental values [13] see the upper structure in Figure 4.14³. Upon hydration the volume of unit cell increases due to an increase in the c -vector, while a - and b -vector changes within 0.05 \AA . See the special case for the hydration of the intercalated Na^+ within Fh_{Na} , upper graph Figure 4.13. The relative error of the lattice angles from 90° is also within 5° , showing a good agreement to assume a monoclinic crystal structure, lower graph in Figure 4.13. Hence assuming further that the interlayer basal spacing d_{001} or the swelling constant, is a good approximation for the c -vector, see the lower structure Figure 4.14.

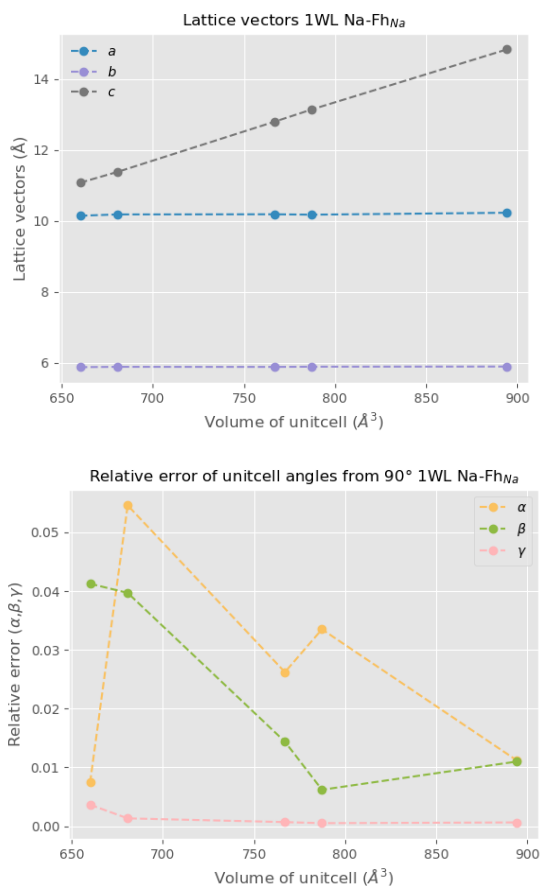
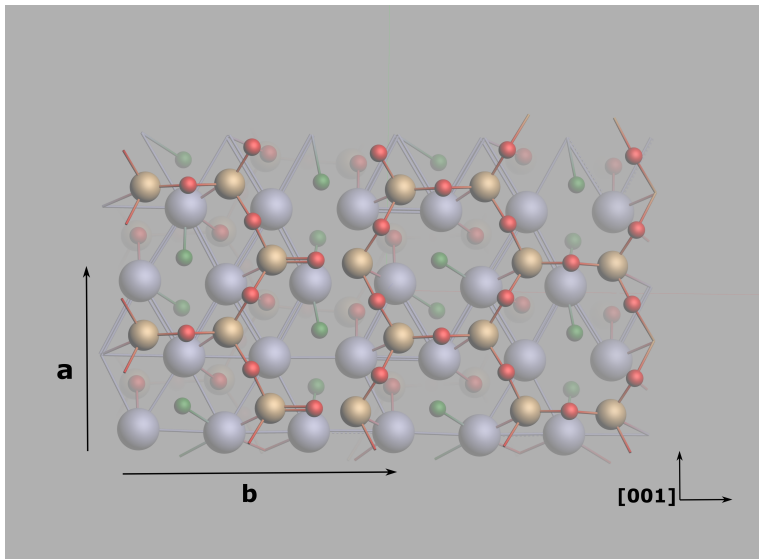
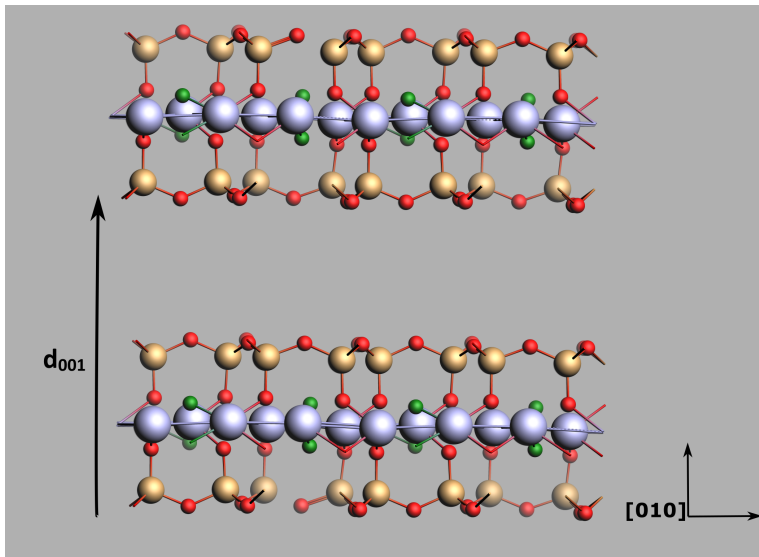


Figure 4.13: Change of lattice parameters upon hydration for the 1WL Na-Fh_{Na} case. Upper graph shows the change in the lattice vectors. While the lower figure measures the relative error from 90° for the lattice angles.

³Pure in this case refers to the case with no substitution of Mg^{2+} in the octahedral layer



(a) The a - and b -vectors projected along $[001]$.



(b) The swelling constant d_{001} viewed from $[010]$.

Figure 4.14: The lattice vectors for plain fluorohectorite.

The swelling properties is strongly controlled by the cation hydration energy, clay composition and layer charge. The case of substitution in the octahedral sheet results in a more delocalized charge distribution, manifested in both "top" and "bottom" of the Fh interlayer surfaces [1, 50]. In contrast to Saponite also a family of smectites, but with substitution in the tetrahedral sheet and thus localized charge only caused on one surface, hence a strong localized adsorption site [1]. From the first calculation of the cation-water complex shows that the metal cations with high hydration energy and small ionic radius, are expected to be more prone to hydration and therefore coordinated to the basal oxygen in a outer sphere coordination(OS). In contrast to cations with large ionic radius and low hydration energies, for instance the K^+ cation with lowest charge to radius ratio for the chosen cations, see Figure 4.9. Known as a swelling inhibitor, and thus remains bound the surface in a inner sphere(IS) coordination [10, 51]. Making K^+ an important special case to consider. Due to recent experiments and simulation work with Na^+ and Ca^{2+} , special attention will also be given to those cations. Thus ranging from cations with large ionic radius and low hydration energy for K^+ , to small ionic radius and high hydration energy for Ca^{2+} .

4.4 Surface charges

To investigate active site of Fh, Bader charge analysis was performed with different cations on the surface for the case of dry Fh_{Li} and Fh_{Na} . Special attention will be given for the hexagonal ring(cavity) of oxygen atoms, depicted in the right structure Figure 4.10. This adsorption site is also reported in the case Na-Fh in the work of Kalo et al. [13]. The atomic charges for the cations and the average charge of the Si and O atoms in the hexagonal cavity are summarized in Table 4.6. As expected for the alkali cations as the ionic radius increases(polarizability) the interaction with the surface is increased in the sequence of $K^+ > Na^+ > Li^+$. Similarly for the divalent cations, with even stronger ionic potential and hence stronger interaction with the surface compared with the monovalent cations. Notice also that cation Fh_{Li} interaction is stronger compared with Fh_{Na} , indicated by the more negative values hence less screening of the hexagonal cavity of oxygens. Which is expected as the Li^+ has larger ionic potential, see Table 4.4. It should be stressed that since the octahedral substitution produce a delocalized charge distribution between the oxygen in the hexagonal cavity, thus symmetry between the upper and lower surface, the charge analysis here are done only for the lower surface (basal surface).

\mathbf{Fh}_{Li}	$\mathbf{M}^{n+}(\text{e})$	$\mathbf{O}(\text{e})$	$\mathbf{Si}(\text{e})$
Li	0.184	-0.269	0.535
Na	0.485	-0.288	0.540
K	0.348	-0.281	0.532
Be	0.256	-0.256	0.551
Mg	0.855	-0.302	0.520
Ca	0.917	-0.304	0.544

Table 4.5: Partial charges of Cations on dry Fh_{Li} . And the average partial charges of Si and O on the interlayer surface. Calculated using Bader charge analysis.

\mathbf{Fh}_{Na}	$\mathbf{M}^{n+}(\text{e})$	$\mathbf{O}(\text{e})$	$\mathbf{Si}(\text{e})$
Li	0.098	-0.271	0.565
Na	0.454	-0.289	0.542
K	0.247	-0.282	0.564
Be	0.298	-0.269	0.576
Mg	0.861	-0.307	0.555
Ca	0.907	-0.305	0.541

Table 4.6: Partial charges of Cations on dry Fh_{Na} . And the average partial charges of Si and O on the interlayer surface. Calculated using Bader charge analysis.

4.5 1WL- and 2WL basal spacing

Since the formation of the IS- or OS(hydration or adsorption) complex depends on the cation-water and cation-surface affinity. The bonding energy and basal spacing d_{001} are calculated as the number of water is increased systematically from 0 to 4 for the 1WL and 0 to 8 for the 2WL. From the first calculation for the only cation-water complex, see section 4.2.2. The binding energy decreases following the sequence $\text{Be}^{2+} > \text{Mg}^{2+} > \text{Ca}^{2+} > \text{Li}^+ > \text{Na}^+ > \text{K}^+$. On the other hand as the polarizability increases the interaction with the surface increases. The calculated interlayer spacing d_{001} for 1WL Fh_{Li} increases with increased number of water molecules for all cations Figure 4.15. Notice a smaller slope for 2-3 water molecule, which correspond to the smallest change in the bonding energy in this region Figure 4.16. This is reasonable for the stable 1WL, compared with suggested $\text{H}_2\text{O}/\text{Na}^+$ ratios of 3.2 experimentally [13]. Notice the samples used experimentally by Kalo et al. had 0.7 Na^+ per formula unit versus 1.0 in this work. Thus reasonable to assume lower number of water molecules to fill the interlayer space.

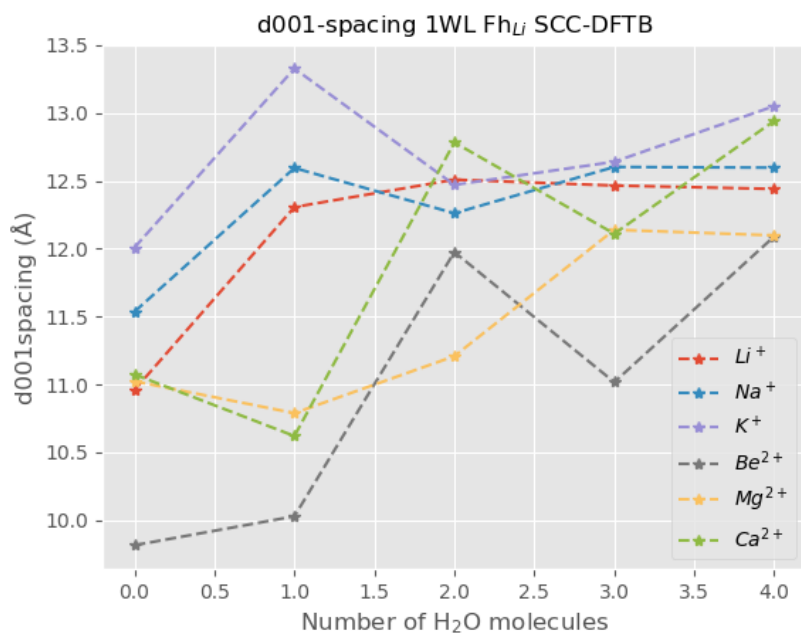


Figure 4.15: Swelling constant d_{001} (Å) 1WL Fh_{Li} as a function of water molecules.

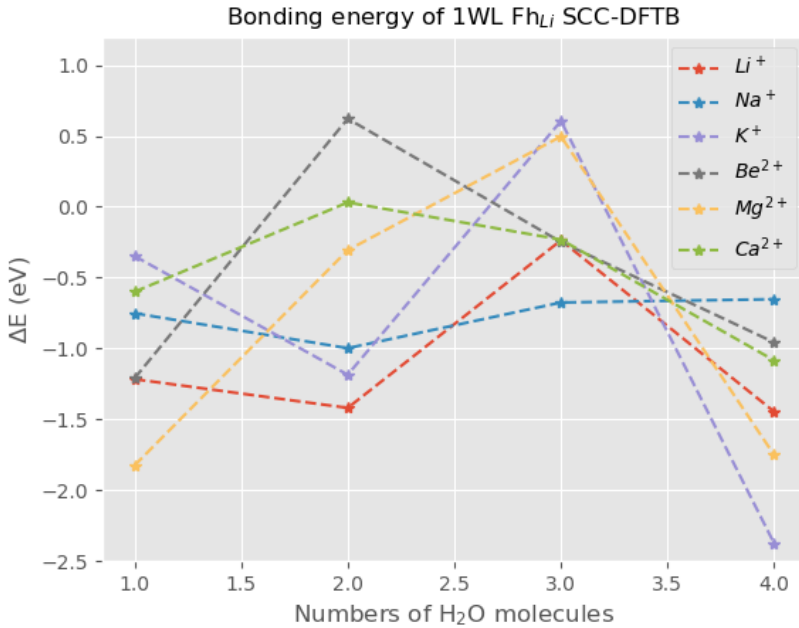


Figure 4.16: Bonding energy of 1WL cation- Fh_{Li} as a function of water molecules.

The case for 2WL shows a clear plateau for 4-6 water molecules, corresponding to a bonding energy minimum with 4 water molecules in the unit cell, see Figure 4.17 and 4.18 respectively. Which is in good agreement with the work by Beyer and von Reichen Bach [49], who used a phlogopite with a layer charge per formula unit of 0.98. And concluded that the ratio $\text{H}_2\text{O}/\text{Na}^+$ of 4 is densely packed for 2WL. This follows the trend for lower number of water molecules compared to experiments done by Kalo et al, with a $\text{H}_2\text{O}/\text{Na}^+$ ratio of 5.6 for the 2WL case. It should be noted that transition is more abrupt for the 2WL case, by comparing the slope of the d_{001} spacing with the case of 1WL above. Clearly from Figure 4.17 the case for 6-8 water molecules in the unit cell correspond to a large energy barrier. Where the added water molecules from 6-8 could describe the case for "intervening" water molecules in the interlayer, without formation of bonds [1]. Detailed discussion of the interaction in the interlayer will follow next in section 4.6.

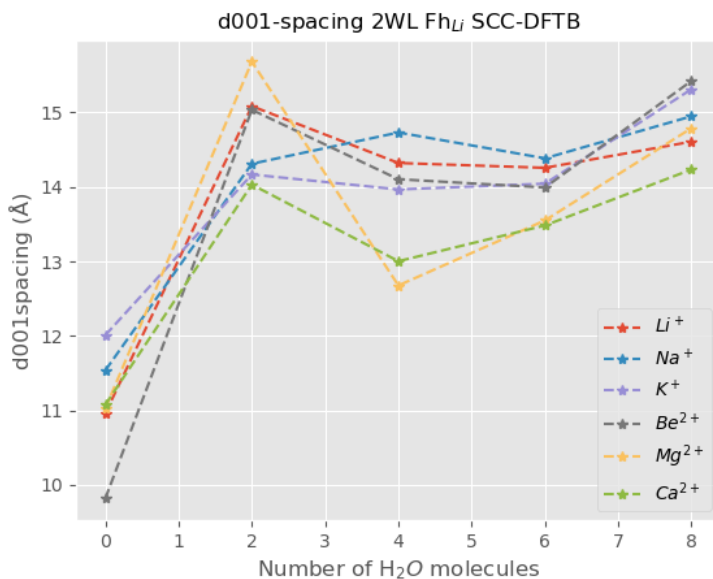


Figure 4.17: Swelling constant d_{001} (Å) of 2WL Fh_{Li} as a function of water molecules.

The computed interlayer spacing of the dehydrated case, 1WL(2 water molecules) and 2WL(4 water molecules) are summarized in Table 4.7 for the case without dispersion correction. For the dry and 1WL Fh_{Li} the basal spacing are systematically overestimated, while the case for 2WL is underestimated. Including the weak interaction between the layers, significantly improves the results for the 1WL state compared with experiments and recent simulations. The inclusion of dispersion correction leads to a shift of ~ 0.5 Å to shorter values. The case for Na in the interlayer shows remarkable agreement with experimental values, see Table 4.8. It should be noted that the calculation without dispersion correction follows best the expected trend, where the interlayer spacing varies linearly with the ionic radius. Which agrees with experiments and simulation for montmorillonites [52]. For the 2WL case the interlayer distance is clearly underestimated by ~ 0.5 Å for Na up to ~ 2.5 Å for Ca. Since the hydration number for the divalent cations is higher, a stable 2WL with 6-8 water molecules in the unit cell could be considered. This is reasonable considering the d_{001} spacing curve in Figure 4.17 showing a basal spacing 13.5-15.3 Å for 6-8 water molecules, hence better agreement with experimental values for the divalent cations. The differences in ratios in the unit cell correlates with the higher charge density and water affinity for the divalent cations. The higher ratios of for instance Ca^{2+}/H_2O compared with Na are also noted in the recent simulation by Loganathan et al. with Ca-hectorite, concluding with a ratio of 9.0 and 16.0 for the stable 1WL and 2WL respectively [48]. Whereas for Na-hectorite they were 3.0 and 10 for the respective 1WL and 2WL [53].

Notice also the simulated values in Table 4.8 from earlier studies, where the hectorite structure was modelled by substituting OH^- with F^- compared with synthetic fluorohectorite in the simulation of this work. This could also be a reason for the low values of the d_{001} spacing. Even though recent experiments with Na-hectorite showed no significant effects of this substitution [53].

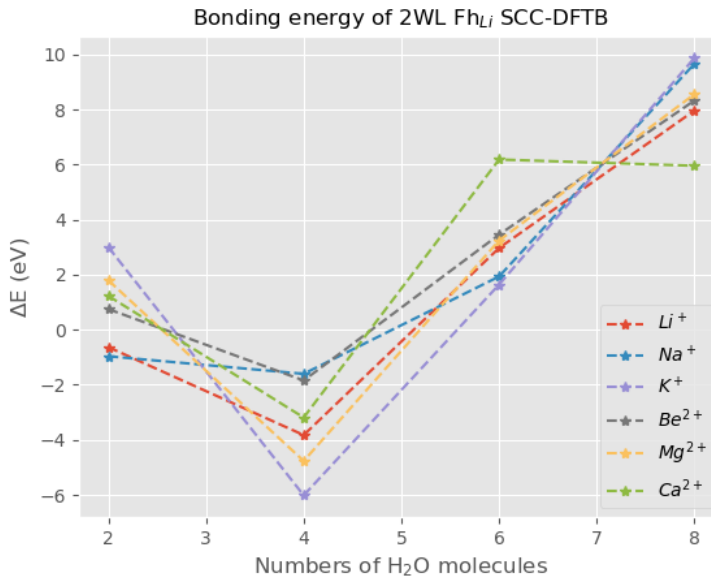


Figure 4.18: Bonding energy of 2WL cation- Fh_{Li} as a function of water molecules.

Previous available experiments have shown that only the 1WL is stable for K^+ in smectite clay [51]. Referred to as a swelling inhibitor. The case for several hydrated states, 2WL or 3WL depends on continuous hydration of the interlayer cation. From the earlier work for the cation-water complex, K had the lowest hydration energy, also observed from the experimental enthalpy of hydration in Table 4.4. And only stable 1WL is observed for Cs, sharing the similar property as K, large ionic radius ($\sim 1.7\text{\AA}$) and low hydration enthalpy (-263kJ/mol) [54]. Which clearly showed a well defined energy barriers between the stable 1WL and the hypothetical 2- and 3WL. Analysis of the 2WL state for K will anyway yield useful dynamical and structural information, which is an inaccessible hypothetical case experimentally.

It should be stressed out at this point that the parametrization of the repulsion term for the parameter set QN15 used by the SCC-DFTB Hamiltonian is experimental [40]. Thus the delicate balance between many terms in the total energy is still a big challenge. Hence the bonding energy curves should rather be taken with caution.

Cation	dry Fh_{Li} (Å)	1WL Fh_{Li} (Å)	2WL Fh_{Li} (Å)
Li	10.96	12.51	14.32
Na	11.53	12.26	14.73
K	12.00	12.47	13.97
Be	9.82	11.95	14.10
Mg	11.02	11.20	12.68
Ca	11.07	12.78	13.00

Table 4.7: Swelling constant d_{001} of Fh_{Li} for the dry, 1WL and 2WL respectively. Without D3(BJ) dispersion correction.

Cation	dry Fh_{Li} (D3-BJ)(Å)	1WL Fh_{Li} (D3-BJ)(Å)	2WL Fh_{Li} (D3-BJ)(Å)
Li	10.44	11.13	13.65
Exp(Li)[12]	-	12.15	15.30
Na	10.03	12.14	14.50
Exp(Na)[13]	9.67	12.45	15.10
Sim(Na)[53]	9.6	11.8	15.2
K	10.90	12.30	14.00
Be	9.70	11.71	12.70
Mg	9.98	11.10	12.60
Ca	11.06	12.58	12.76
Exp(Ca)[55]	12.8	12.8	15.1
Sim(Ca)[48]	9.6	12.3	14.9

Table 4.8: Swelling constant d_{001} of Fh_{Li} for the dry, 1WL and 2WL respectively. With D3(BJ) dispersion correction. Experimental- and simulated work from previous studies are also included.

4.5.1 Basal spacing for Fh_{Na}

Considering the hypothetical case for Fh_{Na} to gain more insight of the underlying principles of the swelling behavior. From the discussion in section 4.4 of the surface charges, the hexagonal cavity for Fh_{Na} is less screened (more negative) by the interlayer cations and thus expecting stronger repulsion of the added water molecules resulting in a larger interlayer spacing for the 1WL and 2WL. But the opposite for the dry structure, greater attraction between the cation and the hexagonal cavity, hence resulting in a smaller interlayer spacing. Following the similar discussion above, the curve for the 1WL d_{001} spacing shows a plateau for the ratio of 2-3 water molecules in the unit cell, see Figure 4.19. The plateau for 3-4 water molecules is reasonable to consider for the divalent cations. Similarly for the Fh_{Li} structure the bonding energy curve shows a minimum for the ratio of 2 water molecules for a stable 1WL.

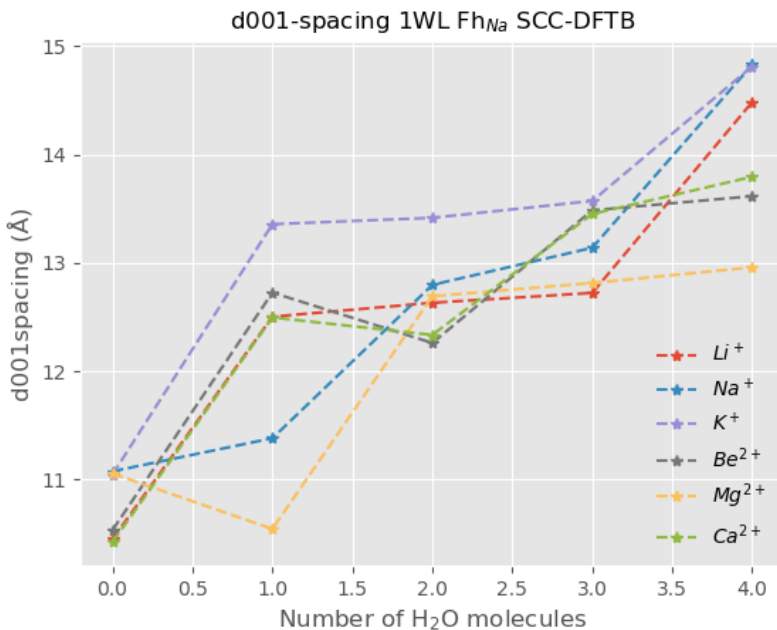


Figure 4.19: Swelling constant d_{001} (Å) of 1WL Fh_{Na} as a function of water molecules.

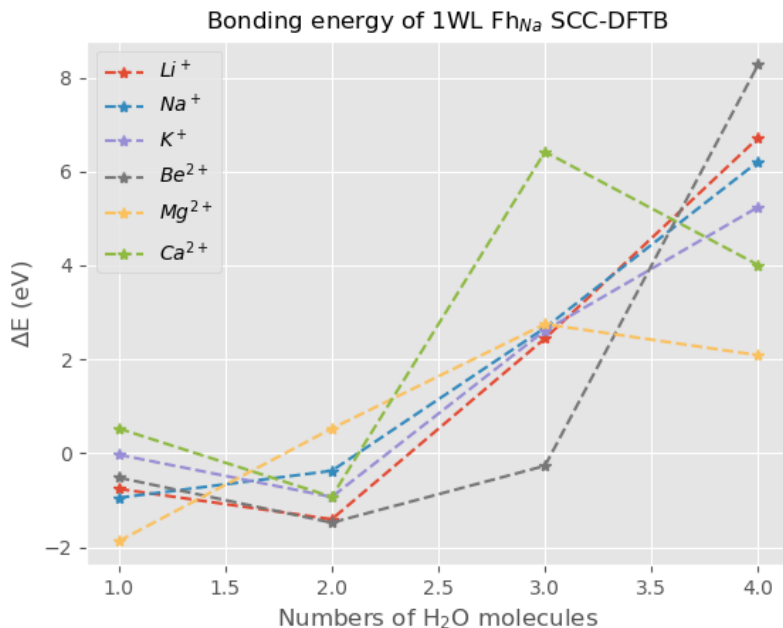


Figure 4.20: Bonding energy of 1WL cation-Fh_{N_a} as a function of water molecules.

Proceeding for the 2WL case, the curve for the d_{001} spacing shows smallest slope going from 4-6 water molecules, in agreement with the case of Fh_{Li}. This again corresponds to the smallest change in the ΔE for the ratio of 4-6 water molecules. And notice also the steeper slope for the added water molecules in the 2WL state, consistent with Fh_{Li}.

Values of the d_{001} spacing are summarized in Table 4.9 without including dispersion correction. The values are consistent with the results for Fh_{Li}. For the dry structure the less screened hexagonal cavity attracts the cation-water complex stronger resulting in a smaller d_{001} compared with Fh_{Li}. For the 1WL and 2WL case, the stronger repulsion between the hexagonal cavity and water molecules, results in a larger d_{001} . Turning on the dispersion correction results in a systematically shorter values of d_{001} , consistent with the results for Fh_{Li}, as weak interaction between the layer sheets are now accounted for.

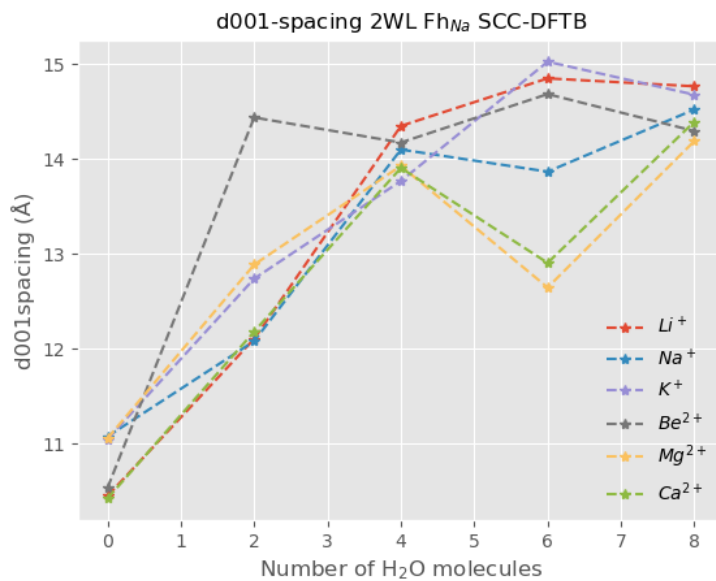


Figure 4.21: Swelling constant d_{001} (Å) of 2WL Fh_{Na} as a function of water molecules.

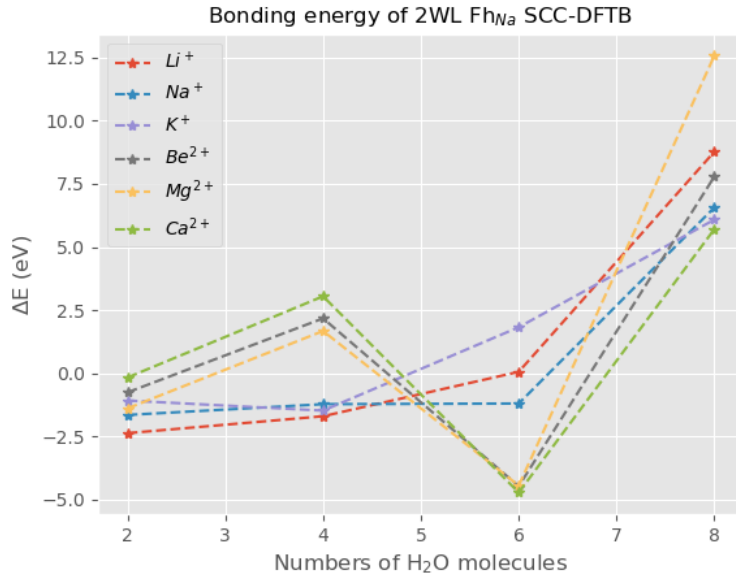


Figure 4.22: Bonding energy of 2WL cation-Fh_{Na} as a function of water molecules.

Cation	dry Fh _{Na} (Å)	1WL Fh _{Na} (Å)	2WL Fh _{Na} (Å)
Li	10.44	12.63	14.34
Na	11.10	12.80	14.10
K	11.00	13.41	13.80
Be	10.53	12.30	14.2
Mg	11.10	12.70	13.92
Ca	10.42	12.33	13.90

Table 4.9: Swelling constant d_{001} of Fh_{Na} for the dry, 1WL and 2WL respectively. Without D3(BJ) dispersion correction.

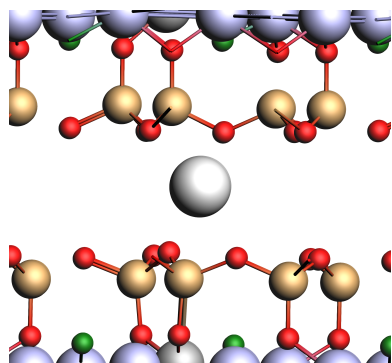
Cation	dry Fh _{Na} (D3-BJ)(Å)	1WL Fh _{Na} (D3-BJ)(Å)	2WL Fh _{Na} (D3-BJ)(Å)
Li	10.20	12.31	14.1
Na	9.77	12.80	13.70
K	10.92	12.33	13.10
Be	10.50	12.21	13.86
Mg	10.93	10.42	13.42
Ca	10.33	12.30	12.60

Table 4.10: Swelling constant d_{001} of Fh_{Na} for the dry, 1WL and 2WL respectively. With D3(BJ) dispersion correction.

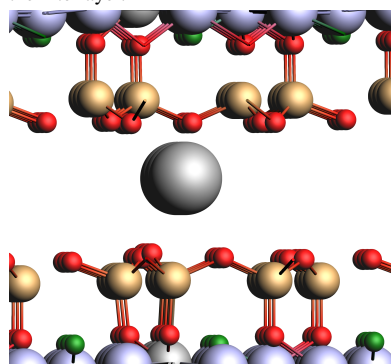
4.6 M^{n+} -H₂O Interlayer Structure

This section presents the results and a comprehensive description of the discussed hydrated states and the interaction between the interlayer species (cation, water and the basal oxygen). The longstanding debate in the literature about the position of the interlayer cations for the 1WL, will be addressed [13, 49]. Following the work by Kalo et al and recent simulations. The results are stressed for Na, Ca and the special case for K. The different cases are for the dry, 1WL and 2WL discussed in the previous section. Corresponding to 0, 2 and 4 water molecules in the unit cell. It should be noted that based only on the bonding energy curve showed no clear energetically well defined states. Since the stability of the interlayer gallery structure depends on the trade offs by many interaction, further discussion of these states will provide more insight.

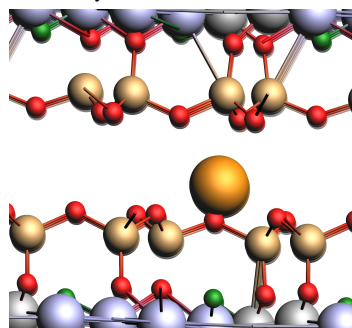
The simulated geometry of the dry M^{n+} -Fh_{Li} are depicted in Figure 4.23, the [010] views the interlayer and the repeated unit cell are projected along the [001] to show the hexagonal cavity. In the dry Na-Fh_{Li}, the Na-O_b distance is 2.43 Å for the closest coordination to basal oxygen atoms. Which correspond to the bond length of 2.35 Å for the cation-water interaction, see Table 4.1. And comparable with experimental values [56]. Where Na⁺ are placed above the Si tetrahedra, shifted towards the hexagonal cavity Figure 4.23b. Coordinated by 4 basal oxygen, in a inner-sphere (IS) coordination. Similarly for the K⁺ cation lies in a IS coordination to basal surface with closest distance of 2.70 Å with O_b, consistent with the 2.65 Å bond length for the K(H₂O)⁺. Due to smaller ionic potential of K⁺ (~0.45) compared with Na⁺ (~0.5), the K cation is less shifted towards the hexagonal cavity Figure 4.23d. While for Ca²⁺ with ionic potential ~2.15 is strongly attracted by the basal surface, placed inside the hexagonal cavity in IS coordination, see Figure 4.23f. With the closest Ca²⁺-O_b of 2.74 Å comparable with Ca²⁺-O bond length of 2.68 Å. These results are consistent with d_{001} spacing for dry Fh_{Li}, where K⁺ had the largest swelling constant of 12.0 Å compared with Na⁺ and Ca²⁺ with d_{001} of 11.5 Å and 11.1 respectively, and correlates with the differences in ionic radius and ionic potential. The data of the coordination structure are summarized in Table 4.11, without inclusion of dispersion correction.



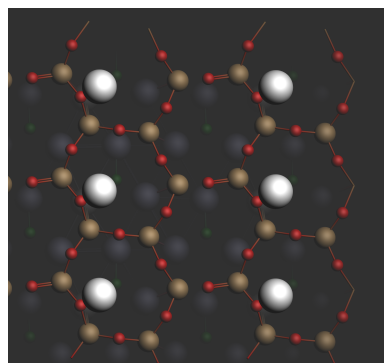
(a) Geometry of dry Na-Fh_{Li}, [010] view of the interlayer.



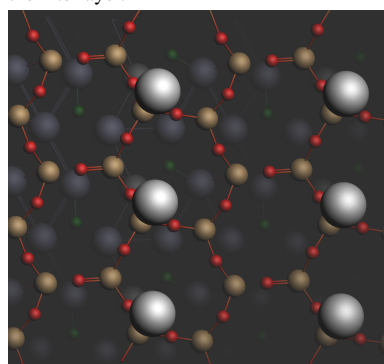
(c) Geometry of dry K-Fh_{Li}, [010] view of the interlayer.



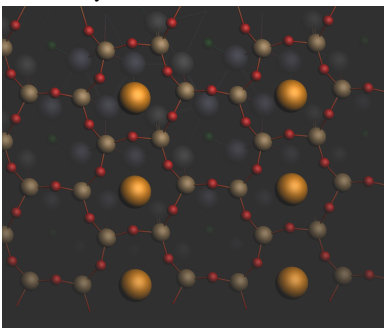
(e) Geometry of dry Ca-Fh_{Li}, [010] view of the interlayer.



(b) Geometry of dry Na-Fh_{Li}, [001] view of the interlayer.



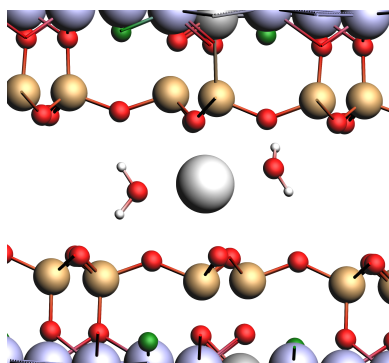
(d) Geometry of dry K-Fh_{Li}, [001] view of the interlayer.



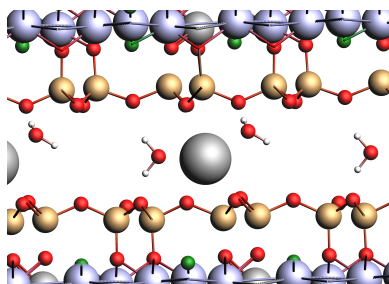
(f) Geometry of dry Ca-Fh_{Li}, [001] view of the interlayer.

Figure 4.23: Geometry of dry Fh_{Li} with Na, K and Ca in the interlayer.

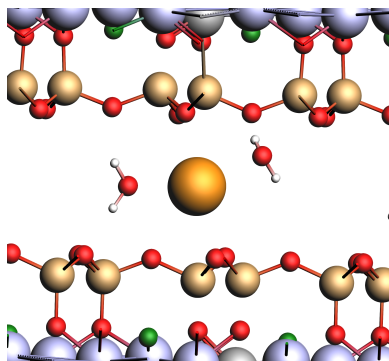
The configuration of the 1WL with two water molecules in the unit cell are depicted Figure 4.24. In the 1WL structure, Na^+ lie in the middle of the interlayer, coordinated by two water molecules and two O_b atoms in a distance of 2.4 Å and 2.6 Å respectively. Corresponding to a symmetric IS coordination with both surfaces, see Figure 4.24a. This partial coordination is consistent with the experimental work of Na-hectorite [13]. Although the work of Kalo et al. showed that the position of Na^+ interlayer cations are shifted towards one of the surfaces, and the Na^+ are placed inside the hexagonal ring. Which could correspond to the different $\text{Na}^+/\text{H}_2\text{O}$ ratios, 3.2 in the experimental work and 2.0 in this simulation. And they reported a semiordered refinement of the 1WL structure. In contrast the K^+ are displaced towards the upper surface, still on the side of hexagonal cavity, see Figure 4.24d. With a K^+-O_b distance of 2.83 Å. Similarly coordinated to 4 oxygen atom, where the average distance to the two water molecules are K^+-O is 2.65, corresponding to the bond length of the K^+ -water complex as expected. Consistent with experimental work, the K^+ cations in IS coordination are shifted more towards the hexagonal cavity, see the [001] projection Figure 4.24d.



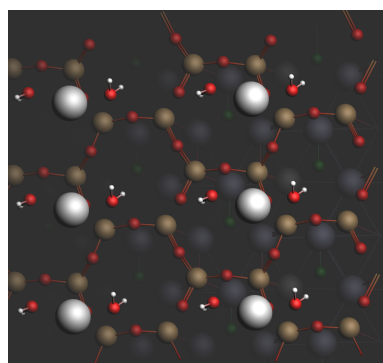
(a) Geometry of 1WL Na-Fh_{Li}, [010] view of the interlayer.



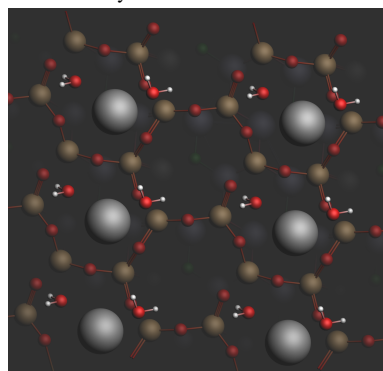
(c) Geometry of 1WL K-Fh_{Li}, [010] view of the interlayer.



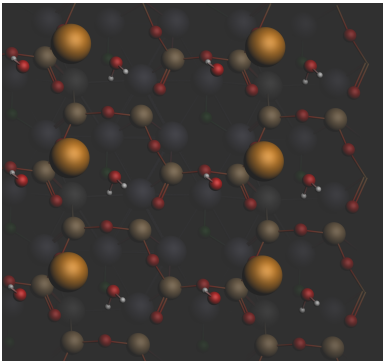
(e) Geometry of 1WL Ca-Fh_{Li}, [010] view of the interlayer.



(b) Geometry of 1WL Na-Fh_{Li}, [001] view of the interlayer.



(d) Geometry of 1WL K-Fh_{Li}, [001] view of the interlayer.

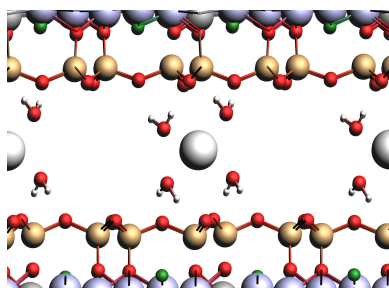


(f) Geometry of 1WL Ca-Fh_{Li}, [001] view of the interlayer.

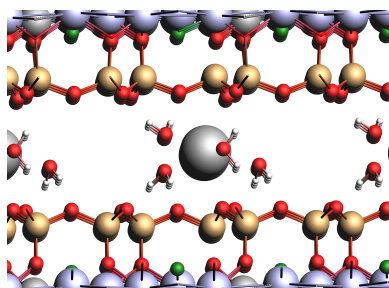
Figure 4.24: Geometry of 1WL Fh_{Li} with Na, K and Ca in the interlayer.

The configuration of the 1WL for Ca^{2+} is similar to K^+ . The Ca^{2+} cations are adsorbed in IS coordination with one surface and OS with the other coordinated by 4 oxygen atoms, see Figure 4.24e. With the Ca^{2+} - O_b distance of 2.74 Å and the average Ca^{2+} -O of 2.7 to the other two water molecules. Which are consistent with the recent simulation of Ca-hectorite by Loganathan et al. showing a distance of 2.8 Å to nearest O_b [48]. Notice the Ca^{2+} resides above the Si tetrahedra and not inside the hexagonal cavity, clearly due to the start of the OS complex formation.

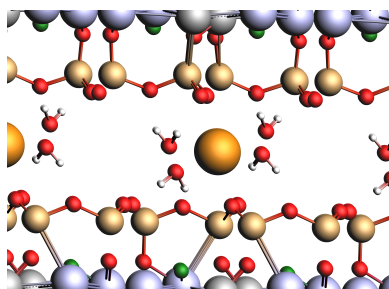
The case for 2WL, with 4 water molecules in the unit cell are depicted in Figure 4.25. The Na^+ in 2WL resides above the tetrahedra in an OS complex coordination, as pointed out by previous experiments and simulation [13][56], see Figure 4.25a. Hydrated by 4 water molecules with average Na^+ -O bond length is 2.44, and as expected longer than the case for 1WL, consistent with the observation that addition of more water molecules is less exothermic in each stage, see section 4.2.2. And the long distance of 3.7 Å to the basal oxygen, therefore not regarded to be part of the coordination sphere. The reported Na^+ -O distance by the simulation of Longanathan et al. is 3.18 Å, coordinated in average by 6.0 water molecules compared to 4.0 in this work. The change of the coordination environments for K^+ in the 2WL case is less significant compared with Na^+ and Ca^{2+} . This is noticed by the K^+ - O_b distance of 2.82 Å compared with K^+ -O distance of 2.75 Å, the small difference indicates that K^+ still forms IS complex with the basal surface, reflecting its small hydration energy. Coordinated by 4 water molecules and one basal oxygen atom. These results are in line with previous studies, showing that K^+ remain bounded to the basal surface, acting as swelling inhibitor [51]. The similar results are observed for Cs^+ , forming IS complex irrespective of the hydration [54]. The Ca^{2+} similar to Na^+ is in only OS coordination by all O_b , with the average Ca^{2+} - O_b distance of 3.3 Å. While the bond length Ca^{2+} -O to the 4 water molecules is 2.72 Å, consistent with the value in bulk solution [57], and with recent simulation [48]. For the 2WL all cations resides above the Si tetrahedra in the middle of the interlayer see Figure 4.25.



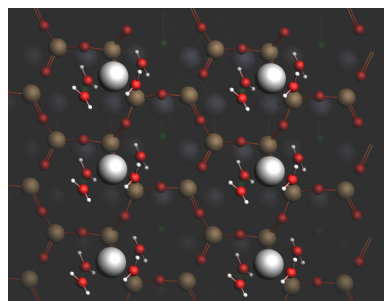
(a) Geometry of 2WL Na-Fh_{Li}, [010] view of the interlayer.



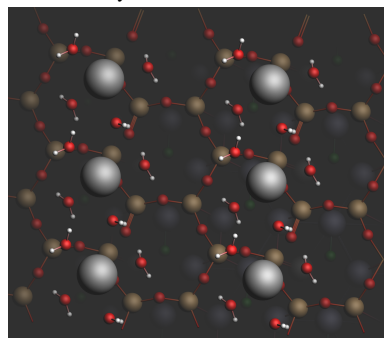
(c) Geometry of 2WL K-Fh_{Li}, [010] view of the interlayer.



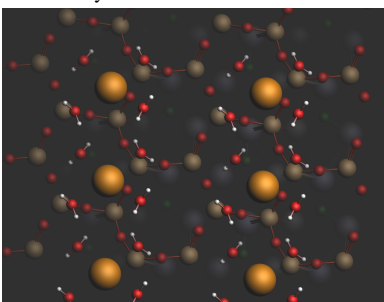
(e) Geometry of 2WL Ca-Fh_{Li}, [010] view of the interlayer.



(b) Geometry of 2WL Na-Fh_{Li}, [001] view of the interlayer.



(d) Geometry of 2WL K-Fh_{Li}, [001] view of the interlayer.



(f) Geometry of 2WL Ca-Fh_{Li}, [001] view of the interlayer.

Figure 4.25: Geometry of 2WL Fh_{Li} with Na, K and Ca in the interlayer.

State	Na ⁺		K ⁺		Ca ²⁺	
	Na ⁺ -O (Å)	Na ⁺ -O _b (Å)	K ⁺ -O (Å)	K ⁺ -O _b (Å)	Ca ²⁺ -O (Å)	Ca ²⁺ -O _b (Å)
Dry Fh _{Li}		2.43		2.70		2.74
1WL Fh _{Li}	2.40	2.56	2.65	2.83	2.70	2.74
2WL Fh _{Li}	2.44	3.68	2.75	2.82	2.72	3.26

Table 4.11: Data of Na⁺, K⁺ and Ca²⁺ coordination structure in dry, 1WL and 2WL Fh_{Li}. Without D3(BJ) dispersion.

State(D3-BJ)	Na ⁺		K ⁺		Ca ²⁺	
	Na ⁺ -O (Å)	Na ⁺ -O _b (Å)	K ⁺ -O (Å)	K ⁺ -O _b (Å)	Ca ²⁺ -O (Å)	Ca ²⁺ -O _b (Å)
Dry Fh _{Li}		2.43		2.70		2.74
1WL Fh _{Li}	2.40	2.52	2.65	2.80	2.70	2.74
2WL Fh _{Li}	2.44	3.58	2.73	2.82	2.72	2.96

Table 4.12: Data of Na⁺, K⁺ and Ca²⁺ coordination structure in dry, 1WL and 2WL Fh_{Li}. With D3(BJ) dispersion correction.

It should be noted for the 2WL state, that the nearest-neighbor(NN) coordination is less than the hydration numbers obtained for the bulk cation-water complex, 4 compared with 6, see Table 4.4. And from the low d_{001} spacing for Ca²⁺ it could be reasonable to consider the case with 3 and 6 water molecules in the unit cell for the 1WL and 2WL states. The cases for 3 and 6 water molecules showed only that the added water molecules formed only second solvation shell, and from frequency calculation these states gave negative eigenvalues, and hence imaginary frequency. From the discussion in section 2.9, this configurations could correspond to a transition state or just a shallow minimum. For that reason they were disregarded in this analysis.

The inclusion of dispersion correction are summarized in Table 4.12. The M^{n+} -O bond length is not effected by the correction, which should be expected. While the M^{n+} -O_b distance is systematically shorter for the different states of hydration, and hence correlated with the sizable shifts of the d_{001} spacing.

5.1 Concluding remarks

A comprehensive study of the hydrated cations in the interlayer of fluorohectorite was simulated using DFT and SCC-DFTB. The monovalent cations (Li^+ , Na^+ and K^+) and the divalent cations (Be^{2+} , Mg^{2+} and Ca^{2+}). Described in the first part using the revPBE functional, the variation of the geometry of water molecules in the first hydration shell upon the change of size and charge of cations. It is shown for the chosen noble-gas like cations that the behavior of the cation-water complex can be reduced to the classical picture of point charge dipole interaction. Where each additional water molecule is less exothermic, and hence the formation of the hydration shell. The Bonding energies ΔE are found to be inversely dependent on the R_{M-O} bond length, given by the linear equation $\Delta E = A(1/R_{M-O}) + B$.

Furthermore the tight-binding method SCC-DFTB for bulk structure of fluorohectorite was used to investigate the microscopic behavior underlying swelling as the water content is systematically increased from 0-4 for the 1WL and 0-8 for the 2WL. The correlation between the bonding energy curve and the d_{001} spacing showed $\text{H}_2\text{O}/M^{n+}$ ratio of 2 and 4 for the stable 1WL and 2WL respectively. The simulated d_{001} spacings for 1WL and 2WL monovalent cations are in remarkable agreement with experimental data. While this value for the 2WL divalent cations was consistently low, indicating a low coordination number. The microscopic interlayer structure revealed that for 1WL Na^+ resides in the middle of the plane shifted towards the hexagonal cavity, in a inner-sphere coordination by both surfaces. While the case for K^+ and Ca^{2+} showed inner-sphere coordination by the basal surface. The interlayer environments for Ca^{2+} and Na^+ changed significantly upon hydration, with only outer-sphere coordination with the basal surface, displaced in the middle plane above the Si tetrahedra. In contrast K^+ remains in a inner-sphere coordination, acting as swelling inhibitor. Reflecting that K^+ screens the negatively charged hexagonal cavity, and hence weakens the repulsion between the clay sheets. Which is in agreement with previous experiments and simulations. The inclusion of the dispersion

correction D3(BJ) improved the agreement of the calculated values of the d_{001} spacing for 1WL by shifting it to shorter values.

5.2 Future work

The correlation between the $M^{n+}-O_b$ and the swelling constant, and the symmetrical delocalized charge distribution of the top and bottom surface of fluorohectorite enables slab modelling of the surface, and hence reducing the computational cost of full DFT simulation. Extending the unit cell to a supercell, thereby looking at larger water-cations ratios, will be a natural step further. The orientation of the water molecules in the interlayer is an important next step to consider the effect of hydrogen bond with the basal oxygen and between water molecules. The effect of this hydrogen bond could also be investigated by vibrational spectra and phonon dispersion curves. Where recent simulation studies showed that the hydrogen bonding network plays a key role in stabilizing the interlayer structure [53, 54]. More challenging case and highly debated are the 1.5 hydration state observed experimentally for Li-Fh, considered as a metastable state [12]. Extensive reasearch for the smectite clays are within CO₂ storage and therefor and interesting case is to consider how the interlayer galleries of interaction are effected by the CO₂ molecules. Where recent experimental studies showed that transition metals like Ni²⁺ is an excellent CO₂ absorbent [8].

Bibliography

- [1] J. Madejova W.J Gates, T. Kloprogge and F. Bergaya. *Infrared and Raman Spectroscopies of Clay Minerals, Volume 8, Elsevier. 2017.*
- [2] R. M Martin. *Electronic structure theory. Cambridge University. 2004.*
- [3] C. J. Giese, R. F.; van Oss. *Colloid and Surface Properties of Clays and Related Minerals; Marcel Dekker: New York, 2002; Vol. 105.*
- [4] Ed Bailey, S. W. *Hydrous Phyllosilicates Mineralogical Society of America: Washington, D.C., 1988; Vol. 19.*
- [5] H.H Murray. *Appl. Clay Sci. 2000, 17, 207.*
- [6] R. D. Cole M. S. Benson. *CO2 Sequestration in Deep Sedimentary Formations. Elements 2008, 4, 325331. 2008.*
- [7] R. C. Ewing J. C. S Long. *Earth-Sciences Issues at a Geological Repository for High-Level Nuclear Waste. Annu. Rev. Earth Planet. Sci. 2004, 32, 363401. 2008.*
- [8] Leide Cavalcanti, Georgios Kalantzopoulos, Juergen Eckert, Kenneth Knudsen, and Jon Fossum. A nano-silicate material with exceptional capacity for co2 capture and storage at room temperature. *Scientific Reports*, 8, 12 2018.
- [9] Éverton Carvalho dos Santos, Zbigniew Rozynek, E. Hansen, Rasmus Hartmann-Petersen, R. Klitgaard, A. Lobner-Olesen, Leander Michels, Alexander Mikkelsen, Tomás Plivelic, Heloisa Bordallo, and Jon Fossum. Ciprofloxacin intercalated in fluorohectorite clay: Identical pure drug activity and toxicity with higher adsorption and controlled release rate. *RSC Advances*, 7:26537–26545, 05 2017.
- [10] D. Bougeard and K. S Smirnov. *Modelling studies of water in crystalline nanoporous aluminosilicates. Phys Chem Chem Phys. 2007 Jan 14;9(2):226-45.*

-
- [11] S. Rosenfeldt M. Stoter and J. Breu. *Tunable Exfoliation of Synthetic Clays*. *Annual Review of Materials Research*. 2015.
- [12] Mario Engelsberg Jon Otto Fossum Fernando Hallwass Rômulo P Tenório, Lars Ramstad Alme. *Geometry and dynamics of intercalated water in Na-fluorhectorite clay hydrates*. 2008.
- [13] W. Milius H. Kalo and J. Breu. *Single crystal structure refinement of one-and two-layer hydrates of sodium fluorohectorite*. *Rsc Advances* , 2(22):8452–8459, 2012. 2012.
- [14] M. M Clark J. A Anthony, A. G. Kalinichev. *Effects of Background Cations on the Fouling of Polyethersulfone Membranes by Natural Organic Matter: Experimental and Molecular Modeling Study*. *J. Membr. Sci.* 2008, 309, 128140.
- [15] W. Kohn. *Electronic Structure of Matter - Wave Functions and Density Functionals*, 93106-9530. 1999.
- [16] Y. Zhao and D. Truhlar. *Density Functionals with Broad Applicability in Chemistry*, *Accounts of chemical research*, vol. 41, pp. 157-167. 2008.
- [17] S. Grimme. *Semiempirical GGA-Type Density Functional Constructed with a LongRange Dispersion Correction*. *Journal of Computational Chemistry*, 27(15):1787-1799, 2006.
- [18] S. Ehrlich S. Grimme, J. Antony and H. Krieg. *A consistent and accurate ab initio parametrization of density functional dispersion correction (DFT-D) for the 94 elements H-Pu*. *The Journal of Chemical Physics*, 132(15):154104, 2010.
- [19] V. Makinen P. Koskinen. *Density-functional tight-binding for beginners*. *Computational materials science* 47, 237 (2009).
- [20] M. Born and R. Oppenheimer. *Zur Quantentheorie der Molekeln*. page 84:457–486, 1927.
- [21] D.R Hartree. *Proceedings of the Royal Society of London*. page A113:621, 1928.
- [22] J. M. Thijssen. *Computational physics*. Cambridge University Press, 1999.
- [23] V. Fock. *Zeitschrift für Physik*. page 61:126, 1930.
- [24] J. Slater. *The theory of complex spectra*, *Physical Review*, vol.34,pp.1293-1322. 1929.
- [25] P. Hohenberg and W. Kohn. *Inhomogeneous Electron Gas*. *Phys. Rev.*,136:B864-B871. 1964.
- [26] P. Hohenberg and W. Kohn. *Physical review*, 136(3B):B864, 1964.
- [27] C.F Fernando N. Miguel and A.L Marques. *A Primer in Density Functional Theory. Lecture Notes in Physics*.2003.
-

-
- [28] L. Hedin and B. I. Lundqvist. *Explicit local exchange-correlation potentials*. *J. Phys. C.*,4(14):2064. 1971.
- [29] C. Kittel. *Introduction to solid state physics*. Wiley. 2005.
- [30] D.C. Langreth and M.J. Mehl. *Physical Review Letters*, B28:1809. 1983.
- [31] J.P. Perdew et al. *Atoms, molecules, solids, and surfaces: Applications of the generalized gradient approximation for exchange and correlation*. *Physical review B*, 46(11):6671-6687,1992.
- [32] K. Burke J.P. Perdew and M. Ernzerhof. *Generalized Gradient Approximation Made Simple*. *Physical Review Letters*, 77(18):3865-3868,1996.
- [33] L. B. Hansen B. Hammer and J. K. Nørskov. *Improved adsorption energetics within density-functional theory using revised Perdew-Burke-Ernzerhof functionals*. *Physical review B*, 59(18):7413, 1999.
- [34] R.P. Feynman. *Forces in molecules*. *Phys. Rev.*, 56:340–343. 1939.
- [35] E. D.; Kong L.; Lundqvist B. I.; Langreth D. C Lee, K.; Murray. *Phys. Rev. B* 2010, 82, 081101.
- [36] Rydberg H. Schröder E. Langreth D. C. Lundqvist Dion, M. *Phys. Rev. Lett.* 2004, 92, 246401.
- [37] D. C.; Lundqvist B. I Andersson, Y.; Langreth. *Phys. Rev. Lett.*1996, 76, 102.
- [38] J.G Brandenburg S. Grimme, A. Hansen and C. Bannwarth. *Dispersion-Corrected Mean-Field Electronic Structure Methods*, *Chemical Reviews* 2016, 116, 9, 5105-5154.
- [39] H.J Monkhorst and J.D Pack. *Electronic structure theory*. Cambridge University. 1976.
- [40] P. Philipsen A. F. Oliveira and T. Heine. *DFTB parameters for the periodic table, part 2: energies and energy gradients from hydrogen to calcium*. *Journal of chemical theory and computation*, 11(11):5209–5218, 2015. 2015.
- [41] *SCM. Basis sets for ADF and BAND*.2010.
- [42] Y. Zhang and W. Yang. *Comment on "Generalized Gradient Approximation Made Simple"*. *Physical Review Letters*, 80(4):890, 1998. 1998.
- [43] A. D. Becke. *A multicenter numerical integration scheme for polyatomic molecules*. *The Journal of Chemical Physics*, 88(4):2547, 1988.
- [44] F. Gahler M. Moseler E. Bitzek, P. Koskinen and P. Gumbsch. *Structural Relaxation Made Simple*,*Phys. Rev. Lett.* 97, 170201 – Published 27 October 2006.
- [45] R. S. Mulliken. *Electronic Population Analysis on LCAO-MO Molecular Wave Functions. I*. *The Journal of Chemical Physics*, 23(10):1833, 1955.

-
- [46] R.F.W Bader. *Atoms in Molecules; a Quantum mechanical theory*. Oxford University Press, 1994.
- [47] Markham G. D. Glusker J. P. George P. Bock Trachtman, M. C. W. *Inorg. Chem.* 1998, 37, 4421–4431.
- [48] G.M. Bowers A.G. Kalinichev R.J. Kirkpatrick N. Loganathan, A.O. Yazaydin. *Cation and Water Structure, Dynamics, and Energetics in Smectite Clays: A Molecular Dynamics Study of Ca–Hectorite*. *The Journal of Physical Chemistry C* 120 (23), 12429-12439. 2016.
- [49] J. Beyer and H. G von Reichenbach. *Clay Miner.*, 2002, 37, 157–168. 2002.
- [50] Josef Breu, Wolfgang Seidl, Alexander Stoll, Kurt Lange, and Thomas Probst. Charge homogeneity in synthetic fluorohectorite. *Chemistry of Materials - CHEM MATER*, 13, 10 2001.
- [51] R. Sutton S. Park A. K Soper J. A. Greathouse G. Sposito, N. T. Skipper. *Surface Geochemistry of Clay Minerals*. *Proc. Natl. Acad. Sci. U. S. A.* 1999, 96, 33583364.
- [52] W.A. Al-Saidi V. K. Voora and K.D Jordan. *Density Functional Theory Study of Pyrophyllite and M-Montmorillonites (M = Li, Na, K, Mg, and Ca): Role of Dispersion Interactions* *The Journal of Physical Chemistry A* 2011 115 (34), 9695-9703.
- [53] A. O.; Krishnan M.; Bowers G. M.; Kalinichev A. G.; Kirkpatrick R. J Morrow, C. P.; Yazaydin. *Structure, Energetics and Dynamics of Smectite Clay Interlayer Hydration: Molecular Dynamics and Metadynamics Investigation of Na-Hectorite*. *J. Phys. Chem. C* 2013, 117, 51725187. 2013.
- [54] A. O.; Bowers G. M.; Kalinichev A. G.; Kirkpatrick R. J. Loganathan, N.; Yazaydin. *Structure, Energetics and Dynamics of Cs+ and H2O in Hectorite: Molecular Dynamics Simulations with a Unconstrained Substrate Surface*. *J. Phys. Chem. C* 2016, 120, 10298. 2016.
- [55] Geoffrey Bowers, Jared Singer, David Bish, and R. Kirkpatrick. Structural and dynamical relationships of ca²⁺ and h₂o in smectite/(h₂o)-h-2 systems. *American Mineralogist*, 99:318–331, 02 2014.
- [56] A. Stoll J. Breu, W. Seidl. *Disorder in Smectites in Dependence of the Interlayer Cation* *Z. Anorg. Allg. Chem.* 2003, 629, 503515.
- [57] J. C.; Lynden-Bell R. M.; Lee S. H. Koneshan, S.; Rasaiah. *Solvent structure, dynamics and the ion mobility in aqueous solution at 25 C*. *J. Phys. Chem. B* 1998, 102, 41934204.